A Mixed-Bouncing Based Non-Stationarity and Consistency 6G V2V Channel Model with Continuously Arbitrary Trajectory

Huang, Ziwei; Bai, Lu ; Sun, Mingran ; Cheng, Xiang; E. Mogensen, Preben; Cai, Xuesong

Published in:
IEEE Transactions on Wireless Communications

DOI:
10.1109/TWC.2023.3293024

2024

A Mixed-Bouncing Based Non-Stationarity and Consistency 6G V2V Channel Model with Continuously Arbitrary Trajectory

Ziwei Huang, *Graduate Student Member, IEEE*, Lu Bai, *Member, IEEE*, Mingran Sun, *Graduate Student Member, IEEE*, Xiang Cheng, *Fellow, IEEE*, Preben E. Mogensen, *Member, IEEE*, and Xuesong Cai, *Senior Member, IEEE*

***Abstract*—In this paper, a novel three-dimensional (3D) irregular shaped geometry-based stochastic model (IS-GBSM) is proposed for sixth-generation (6G) millimeter wave (mmWave) massive multiple-input multiple-output (MIMO) vehicle-to-vehicle (V2V) channels. To investigate the impact of vehicular traffic density (VTD) on channel statistics, clusters are divided into static clusters and dynamic clusters, which are further distinguished into static/dynamic single/twin-clusters to capture the mixed-bouncing propagation. A new method, which integrates the visibility region and birth-death process methods, is developed to model space-time-frequency (S-T-F) non-stationarity of V2V channels with time-space (T-S) consistency. The continuously arbitrary vehicular movement trajectory (VMT) and soft cluster power handover are modeled to further ensure channel T-S consistency. From the proposed model, key channel statistics are derived. Simulation results show that S-T-F non-stationarity of channels with T-S consistency is modeled and the impacts of VTD and VMT on channel statistics are analyzed. The generality of the proposed model is validated by comparing simulation results and measurement/ray-tracing (RT)-based results.**

***Index Terms*—6G vehicle-to-vehicle (V2V) channel model, space-time-frequency (S-T-F) non-stationarity, time-space (T-S) consistency, continuously arbitrary trajectory, mixed-bouncing propagation.**

I. Introduction

ONE key technology of the intelligent transportation system is the vehicle-to-vehicle (V2V) communication, which can facilitate diverse applications. In the upcoming sixth-generation (6G) era, V2V communication system needs to meet the demands of significantly low latency, high throughput, as well as high reliability. Towards this objective, massive multiple-input multiple-output (MIMO) and millimeter wave (mmWave) technologies should be employed in the 6G V2V system. For a proper design and performance evaluation of 6G V2V systems, realistic and easy-to-use 6G V2V channel models need to be developed [1].

V2V communications are extremely dynamic, where transmitter (Tx), receiver (Rx), and the surrounding vehicles are moving at high speed. The *actual V2V propagation environment* has two unique features, i.e., various vehicular traffic densities (VTDs) and complex vehicular movement trajectories (VMTs), and a distinctive scattering environment (SE), i.e., the existence of mixed-bouncing propagation and ground reflection (GR), which distinctly effect the channel statistics according to the measurement and analysis [2]–[6]. First, V2V channels exhibit different channel statistics in high/low VTD, which represents the high/low ratio of the number of mobile vehicles, i.e., dynamic clusters, to the number of static buildings and trees, i.e., static clusters. Second, VMTs are diverse and channel statistics are different under different VMTs. Third, due to rapidly-changing and complicated V2V communication scenarios, both the single-bouncing and multi-bouncing, i.e., mixed-bouncing propagation, and the GR component exist.

To capture the actual V2V propagation environment, many V2V geometry-based stochastic models (GBSMs) have been developed, which can be divided into the regular shaped-GBSMs (RS-GBSMs) and irregular shaped-GBSMs (IS-GBSMs). In RS-GBSMs, clusters are placed on regular shapes, e.g., ellipsoid, cylinder, semi-sphere, etc. [7]. In IS-GBSMs, the position of clusters follows a certain statistical distribution [8], [9]. Owing to the excellent trade-off between complexity and accuracy, the modeling approach of IS-GBSM has been widely adopted in the standardized channel modeling [10].

In the V2V IS-GBSM [11], the clusters were divided into static and dynamic clusters and the influence of VTD on channel statistics was analyzed. Nonetheless, the VMTs of transceivers were discontinuous, uniform, and rectilinear. To address this limitation, a V2V IS-GBSM in [12] modeled the continuously various VMTs by considering the acceleration vector and integral operation, while the values of transceiver

Manuscript received October 12, 2022; revised January 25, 2023 and April 18, 2023; accepted June 28, 2023. This work was supported in part by the National Natural Science Foundation of China (Grants No. 62125101, 62341101, and 62001018), the Horizon Europe Framework Programme under the Marie Skłodowska-Curie grant agreement No.,101059091, the Swedish Research Council (Grant No. 2022-04691), and the strategic research area ELLIIT, Excellence Center at Linköping — Lund in Information Technology. The review of this article was coordinated by Prof. Yue Gao. *(Corresponding author: Xiang Cheng.)*

Z. Huang, M. Sun, and X. Cheng are with the State Key Laboratory of Advanced Optical Communication Systems and Networks, School of Electronics, Peking University, Beijing 100871, P. R. China, and also with the Henan Joint International Research Laboratory of Intelligent Networking and Data Analysis, Zhengzhou University, Zhengzhou 450001, P. R. China (email: ziweihuang@pku.edu.cn, mingransun_pku@163.com, xiangcheng@pku.edu.cn).

L. Bai is with the Joint SDU-NTU Centre for Artificial Intelligence Research (C-FAIR), Shandong University, Jinan 250101, P. R. China (e-mail: lubai@sdu.edu.cn).

P. E. Mogensen is with the Department of Electronic Systems, Aalborg University, Aalborg 9220, Denmark, and also with Nokia, Aalborg 9220, Denmark (e-mail: pm@es.aau.dk).

X. Cai is with the Department of Electrical and Information Technology, Lund University, Lund 22100, Sweden (e-mail: xuesong.cai@eit.lth.se).

velocities were constant. The authors in [13] developed a MIMO sub-6 GHz vehicular IS-GBSM, which mimicked the arbitrary VMTs and dynamic clusters via the time-variant acceleration and the random walk process, respectively. However, the aforementioned IS-GBSMs in [11]–[13] cannot model the mixed-bouncing propagation. The IS-GBSMs in [11] and [12] exploited the method of twin-clusters to model the multi-bouncing propagation. Nevertheless, the angle of departure (AoD) via the twin-cluster nearby Tx and the angle of arrival (AoA) via the twin-cluster nearby Rx were uncorrelated, which cannot imitate the single-bouncing propagation. Conversely, the IS-GBSM in [13] solely captured the single-bouncing propagation by generating single reflection clusters, named as single-clusters in this paper. In [14], a general IS-GBSM was proposed to attempt to imitate the mixed-bouncing propagation, whereas the GR component was ignored. To overcome this limitation, the IS-GBSM in [15] considered the GR component and attempted to develop a mixed-bouncing based IS-GBSM. However, in the IS-GBSMs [14], [15], the effect of the ratio of single-bouncing via single-clusters to multi-bouncing via twin-clusters on channel statistics was ignored. Note that, the adequate modeling of mixed-bouncing propagation needs to simultaneously capture the single/multi-bouncing propagation and analyze the impact of the ratio between them on channel statistics. The unique features, i.e., various VTDs and complex VMTs, of V2V communications were also neglected in the IS-GBSMs [14], [15]. Therefore, a V2V channel model, which can capture the actual V2V propagation environment, including VTD, VMT, mixed-bouncing propagation, and GR component, is still lacking.

In the upcoming 6G, when massive MIMO and mmWave technologies are applied to highly dynamic V2V scenarios, channels will exhibit space-time-frequency (S-T-F) non-stationarity. Channel non-stationarity is an essential channel characteristic and channel non-stationarity in a particular domain, such as space/time/frequency, represents that channel statistical properties vary in this domain [16]. As mentioned in [3], [6], channels under massive MIMO, high-mobility communication scenarios, and massive MIMO exhibit space, time, and frequency non-stationarity, respectively. To model S-T-F non-stationarity, a V2V IS-GBSM was developed in [17], which integrated the improved K-Means clustering algorithm and birth-death process method to model the correlated cluster based array-time evolution. However, the IS-GBSM in [17] ignored the capturing of time-space (T-S) consistency, which is an inherent channel physical feature. Channel consistency in the space/time domain means that the channel varies smoothly and consistently as the array/time evolves. When massive MIMO and mmWave technologies are utilized in high-mobility communication scenarios, it is exceedingly necessary to capture channel consistency [6]. The emergence of integrated sensing and communication (ISAC) systems further results in the necessity of capturing T-S consistency [18]. Unlike [10], [19], this paper makes a more strict distinction of channel consistency similarly to [18]. Specifically, since the space domain refers to the antenna array domain with the advent of MIMO technology, T-S consistency represents that the channel changes smoothly as time-array evolves. In [20], a general IS-GBSM was proposed to capture S-T-F non-stationarity and time consistency by exploiting the birth-death process and tracking the locations of transceivers and clusters. In the European COoperation in the field of Scientific and Technical research (COST) 2100 channel model [21], a different method, named as the visibility region, was proposed to mimic channel non-stationarity and consistency. By modeling the smooth cluster evolution as clusters move in and out of visibility region, time non-stationarity and consistency were captured. However, both the IS-GBSMs in [20], [21] cannot model S-T-F non-stationarity with T-S consistency. To overcome this drawback, our previous work in [18] developed a general S-T-F non-stationary IS-GBSM with T-S consistency. In [18], the visibility region method was applied to the array-time axis and a frequency-dependent factor was developed. Nonetheless, the unique features, i.e., various VTDs and complex VMTs, and distinctive SE, i.e., mixed-bouncing propagation and GR component, of V2V communications were disregarded, which affect the modeling of S-T-F non-stationarity with T-S consistency. Currently, a method that has the capability to integrate the modeling of S-T-F non-stationarity with T-S consistency and the capturing of actual V2V propagation environment is still lacking.

To fill the above gaps, a novel 6G V2V massive MIMO mmWave IS-GBSM is proposed. The proposed IS-GBSM can be regarded as a 6G channel model by modeling S-T-F non-stationarity of channels with T-S consistency in consideration of the impacts of VTD, continuously arbitrary VMTs, and mixed-bouncing propagation. Based upon the proposed IS-GBSM, the capturing and investigation of the S-T-F non-stationarity and T-S consistency can provide valuable suggestion for designing the 6G V2V system. Additionally, the proposed IS-GBSM is used as a simulation and validation platform to support the design of 6G V2V system algorithms. The major contributions and novelties of this paper are summarized as follows.

1) A new S-T-F non-stationarity and T-S consistency IS-GBSM with continuously arbitrary VMTs, GR component, and mixed-bouncing propagation for 6G massive MIMO mmWave V2V channels is proposed. From the proposed model, key channel statistics are obtained.
2) To model the mixed-bouncing propagation and describe the V2V scenarios with different VTDs, clusters are divided into static/dynamic clusters and single/twin-clusters. Two indexes are given to quantitatively characterize the ratios of the numbers of static/dynamic and single/twin-clusters. Continuously arbitrary VMTs of dynamic clusters and transceivers are further mimicked by the integration of time and time-varying acceleration.
3) A new method, which can model S-T-F non-stationarity with T-S consistency in consideration of the effects of VTD, continuously arbitrary VMT, and mixed-bouncing propagation, is developed for the first time. The developed method integrates the visibility region and birth-death process methods. A soft transition factor and a frequency-dependent factor are proposed to capture the soft cluster power handover and frequency non-

stationarity, respectively.

4) Simulation results show that the proposed model can mimic S-T-F non-stationarity of channels with T-S consistency, and the impacts of two indexes on channel statistics are explored. By comparing simulation results and measurement/ray-tracing (RT)-based results, the utility of the proposed model is verified.

The remainder of this paper is organized as follows. In Section II, the framework of the proposed model is elaborated. Section III describes the developed S-T-F non-stationarity of V2V channels with T-S consistency modeling method. In Section IV, typical channel statistical properties are given. In Section V, the simulation result is presented and further compared with the measurement/RT-based results. Finally, conclusions are presented in Section VI.

II. Framework of the Proposed Channel Model

The V2V communication system is equipped with uniform linear antenna array with $M_{\mathrm{T}}/M_{\mathrm{R}}$ antennas at Tx/Rx, where adjacent antenna spacing is $\delta_{\mathrm{T}}/\delta_{\mathrm{R}}$. In Fig. 1, the geometrical representation of proposed IS-GBSM is elaborated, where the angle information is omitted for clarity. The p/q-th antenna in the Tx/Rx array is $A_p^{\mathrm{T}}/A_q^{\mathrm{R}}$. To mimic the continuously arbitrary VMT, the time-variant acceleration is introduced in the transceiver velocity. The corresponding velocity vector is $\mathbf{v}^{\mathrm{T/R}}(t)=[v_{\mathrm{x}}^{\mathrm{T/R}}(t),v_{\mathrm{y}}^{\mathrm{T/R}}(t),0]^{\mathrm{T}}$ with

$$v_{\mathrm{x/y}}^{\mathrm{T/R}}(t)=v_{\mathrm{x/y}}^{\mathrm{T/R}}(0)+\int_0^t a_{\mathrm{x/y}}^{\mathrm{T/R}}(t)\mathrm{d}t \tag{1}$$

where $v_{\mathrm{x/y}}^{\mathrm{T/R}}(0)$ is the velocity of Tx/Rx at initial time. The distance between the center of transceivers is $D_{\mathrm{cen}}(t)$.

To consider the impact of VTD, clusters are divided into static/dynamic clusters according to whether the cluster velocity is zero. To mimic the mixed-bouncing propagation, clusters are further separated as single-clusters and twin-clusters. In Fig. 1, the link bounces from Tx to Rx once, i.e., single-bouncing propagation, via a single-cluster. Unlike single-clusters, the twin-cluster consists of a sub-cluster nearby Tx and a sub-cluster nearby Rx, which characterize the first bounce and the last bounce, respectively. Bounces between the twin-clusters are abstracted as a virtual link. Therefore, twin-clusters can capture the multi-bouncing propagation. There are four types of clusters, including static single-clusters, static twin-clusters, dynamic single-clusters, and dynamic twin-clusters, and their numbers are $S(t)$, $I(t)$, $D(t)$, and $J(t)$, respectively. The s/d-th static/dynamic single-cluster is $C_{s/d}^{\mathrm{SS}}$, and the i/j-th static/dynamic twin-cluster nearby Tx/Rx is $C_{i/j}^{\mathrm{DM,T/R}}$. A scattering density index $\epsilon_{\mathrm{SDI}}(t)$ is given to characterize the ratio of the numbers of single-clusters to twin-clusters, i.e., $\epsilon_{\mathrm{SDI}}(t)=\frac{S(t)+D(t)}{I(t)+J(t)}$. In the sparse SE, the value of scattering density index is large. A vehicle density index $\epsilon_{\mathrm{VDI}}(t)$ is given to represent the ratio of the numbers of static clusters to dynamic clusters, i.e., $\epsilon_{\mathrm{VDI}}(t)=\frac{S(t)+I(t)}{D(t)+J(t)}$. In the low VTD scenario, the value of vehicle density index is large. In addition to modeling the impacts of VTD and SE, the proposed model also considers the mmWave communication. The communication under the high frequency band can provide high data rate transmission and has been widely used [22], [23]. To imitate the high delay resolution in mmWave communications, there are $N_s(t)$, $N_i(t)$, $N_d(t)$, and $N_j(t)$ rays within the clusters C_s^{SS}, $C_i^{\mathrm{SM,T/R}}$, C_d^{DS}, and $C_j^{\mathrm{DM,T/R}}$, respectively. To support the continuously arbitrary VMT, the time-varying acceleration is introduced into the velocity vectors of dynamic clusters C_d^{DS} and $C_j^{\mathrm{DM,T/R}}$, i.e., $\mathbf{v}_d^{\mathrm{DS}}(t)$ and $\mathbf{v}_j^{\mathrm{DM,T/R}}(t)$, which are calculated similarly to (1).

A. Complex Channel Gain of LoS Component

The complex channel gain of line-of-sight (LoS) component related to the sub-channel between the Tx antenna $\mathrm{A}_p^{\mathrm{T}}$ and the Rx antenna $\mathrm{A}_q^{\mathrm{R}}$, is given by

$$h_{qp}^{\mathrm{LoS}}(t)=Q_{T_{\mathrm{E}}}(t)\exp\left\{j2\pi\int_0^t f_{qp}^{\mathrm{LoS}}(t)\mathrm{d}t+j\varphi_{qp}^{\mathrm{LoS}}(t)\right\} \tag{2}$$

where T_{E} denotes an observation time interval and $Q_{T_{\mathrm{E}}}(t)$ represents a rectangular window function, which is given as $Q_{T_{\mathrm{E}}}(t)=\begin{cases}1, & 0\leqslant t\leqslant T_{\mathrm{E}},\\ 0, & \text{otherwise.}\end{cases}$. The delay, phase shift, as well as Doppler shift related to LoS component are $\tau_{qp}^{\mathrm{LoS}}(t)=\frac{\left\|\mathbf{D}_{qp}^{\mathrm{LoS}}(t)\right\|}{c}$, $\varphi_{qp}^{\mathrm{LoS}}(t)=\varphi_0+\frac{2\pi}{\lambda}\left\|\mathbf{D}_{qp}^{\mathrm{LoS}}(t)\right\|$, and $f_{qp}^{\mathrm{LoS}}(t)=\frac{1}{\lambda}\frac{\left\langle\mathbf{D}_{qp}^{\mathrm{LoS}}(t),\mathbf{v}^{\mathrm{R}}(t)-\mathbf{v}^{\mathrm{T}}(t)\right\rangle}{\left\|\mathbf{D}_{qp}^{\mathrm{LoS}}(t)\right\|}$, respectively. Then, c represents the speed of light, λ is the carrier wavelength, and φ_0 denotes the initial phase shift. $\langle\cdot,\cdot\rangle$ and $\|\cdot\|$ denote the inner product and Frobenius norm, respectively. $\mathbf{D}_{qp}^{\mathrm{LoS}}(t)$ is the distance vector from antennas $\mathrm{A}_p^{\mathrm{T}}$ to $\mathrm{A}_q^{\mathrm{R}}$ and is written as

$$\mathbf{D}_{qp}^{\mathrm{LoS}}(t)=\mathbf{D}_{qp}^{\mathrm{LoS}}(0)-\int_0^t\mathbf{v}^{\mathrm{T}}(t)\mathrm{d}t+\int_0^t\mathbf{v}^{\mathrm{R}}(t)\mathrm{d}t \tag{3}$$

where $\mathbf{D}_{qp}^{\mathrm{LoS}}(0)$ is the distance vector from the antennas $\mathrm{A}_p^{\mathrm{T}}$ to $\mathrm{A}_q^{\mathrm{R}}$ at initial time.

B. Complex Channel Gain of NLoS Component via Ground Reflection

The complex channel gain of GR component is written as

$$\begin{aligned}h_{qp}^{\mathrm{GR}}(t)=&Q_{T_{\mathrm{E}}}(t)\sqrt{P^{\mathrm{GR}}(t)}\\&\times\exp\left\{j2\pi\left[\int_0^t f_p^{\mathrm{GR,T}}(t)\mathrm{d}t+\int_0^t f_q^{\mathrm{GR,R}}(t)\mathrm{d}t\right]+j\varphi_{qp}^{\mathrm{GR}}(t)\right\}\end{aligned} \tag{4}$$

where $P^{\mathrm{GR}}(t)$ is the power of GR component. The delay, phase shift, and Doppler shift of GR component related to the Tx antenna $\mathrm{A}_p^{\mathrm{T}}$ and the Rx antenna $\mathrm{A}_q^{\mathrm{R}}$ are $\tau_{qp}^{\mathrm{GR}}(t)=\frac{\|\mathbf{D}_p^{\mathrm{GR,T}}(t)\|+\|\mathbf{D}_q^{\mathrm{GR,R}}(t)\|}{c}$, $\varphi_{qp}^{\mathrm{GR}}(t)=\varphi_0+\frac{2\pi}{\lambda}\left(\|\mathbf{D}_p^{\mathrm{GR,T}}(t)\|+\|\mathbf{D}_q^{\mathrm{GR,R}}(t)\|\right)$, and $f_{p/q}^{\mathrm{GR,T/R}}(t)=\frac{1}{\lambda}\frac{\left\langle\mathbf{D}_{p/q}^{\mathrm{GR,T/R}}(t),\mathbf{v}^{\mathrm{T/R}}(t)\right\rangle}{\|\mathbf{D}_{p/q}^{\mathrm{GR,T/R}}(t)\|}$, respectively. $\mathbf{D}_{p/q}^{\mathrm{GR,T/R}}(t)$ denotes the distance vector from the Tx/Rx antenna $\mathrm{A}_{p/q}^{\mathrm{T/R}}$ to the GR point and its computation is presented below. First, based on Fig. 2, the azimuth distance between Tx and GR point is $\chi_{\mathrm{T}}(t)=\frac{\xi_{\mathrm{T}}}{\xi_{\mathrm{T}}+\xi_{\mathrm{R}}}\|\mathbf{D}_{\mathrm{cen}}(t)\|$, where ξ_{T} and ξ_{R} are ground clearances of Tx and Rx. Second, based on the geometrical relationship, the distance from Tx to GR point is $\|\mathbf{D}_{\mathrm{cen}}^{\mathrm{GR,T}}(t)\|=\sqrt{\chi_{\mathrm{T}}^2(t)+\xi_{\mathrm{T}}^2}$ and the distance from GR point to Rx is $\|\mathbf{D}_{\mathrm{cen}}^{\mathrm{GR,R}}(t)\|=$

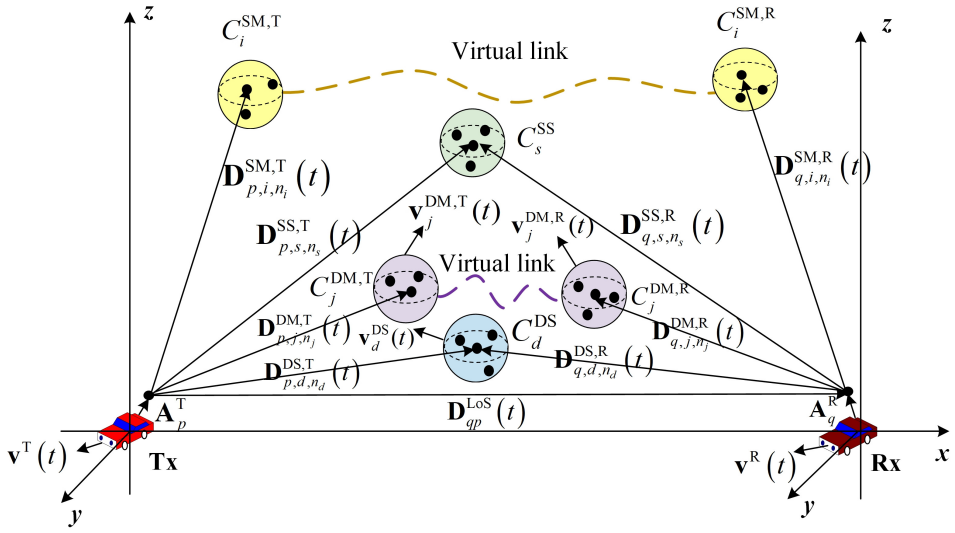

Fig. 1. Geometrical representation of the proposed 6G V2V massive MIMO mmWave IS-GBSM.

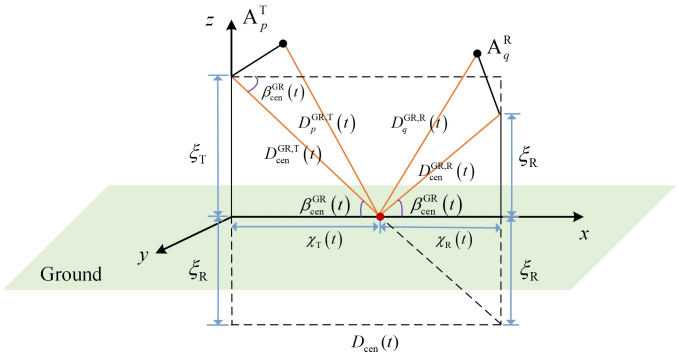

Fig. 2. Geometrical relationship related to the GR component.

$\sqrt{\|\mathbf{D}_{\text{cen}}(t)\|^2+(\xi_{\text{T}}+\xi_{\text{R}})^2}-\|\mathbf{D}_{\text{cen}}^{\text{GR,T}}(t)\|$. Third, the distance vector $\mathbf{D}_{\text{cen}}^{\text{GR,T/R}}(t)$ is expressed by

$$\mathbf{D}_{\text{cen}}^{\text{GR,T/R}}(t)=\|\mathbf{D}_{\text{cen}}^{\text{GR,T/R}}(t)\|\begin{bmatrix}\cos\beta_{\text{cen}}^{\text{GR}}(t)\cos\alpha_{\text{cen}}^{\text{GR}}(t)\\ \cos\beta_{\text{cen}}^{\text{GR}}(t)\sin\alpha_{\text{cen}}^{\text{GR}}(t)\\ \sin\beta_{\text{cen}}^{\text{GR}}(t)\end{bmatrix} \tag{5}$$

where $\alpha_{\text{cen}}^{\text{GR}}(t)$ and $\beta_{\text{cen}}^{\text{GR}}(t)$ denote azimuth and elevation angles of the distance vector $\mathbf{D}_{\text{cen}}^{\text{GR,T/R}}(t)$, respectively. Based on [24], only the elevation angle of distance vector $\mathbf{D}_{\text{cen}}^{\text{GR}}(t)$ needs to be taken into account and is given as $\beta_{\text{cen}}^{\text{GR}}(t)=\arctan\frac{\xi_{\text{R}}}{\chi_{\text{R}}(t)}$. Fourth, the distance vectors from antennas A_p^{T} and A_q^{R} to the GR point are calculated by $\mathbf{D}_p^{\text{GR,T}}(t)=\mathbf{D}_{\text{cen}}^{\text{GR,T}}(t)-\mathbf{A}_p^{\text{T}}$ and $\mathbf{D}_q^{\text{GR,R}}(t)=\mathbf{D}_{\text{cen}}^{\text{GR,R}}(t)-\mathbf{A}_q^{\text{R}}$.

C. Complex Channel Gain of NLoS Components via Static Single-Clusters and Twin-Clusters

In this subsection, the complex channel gain of non-line-of-sight (NLoS) components via static single/twin-clusters is derived.

1) Static Single-Clusters: The complex channel gain of the sub-channel related to the Tx antenna A_p^{T} and the Rx antenna A_q^{R} via the n_s-th ray within the cluster C_s^{SS} is written by

$$h_{qp,s,n_s}^{\text{SS}}(t)=Q_{T_{\text{E}}(t)}\sqrt{P_{s,n_s}^{\text{SS}}(t)}\times\exp\left\{j2\pi\left[\int_0^t f_{p,s,n_s}^{\text{SS,T}}(t)\text{d}t+\int_0^t f_{q,s,n_s}^{\text{SS,R}}(t)\text{d}t\right]+j\varphi_{qp,s,n_s}^{\text{SS}}(t)\right\} \tag{6}$$

where $P_{s,n_s}^{\text{SS}}(t)$ is the power of the n_s-th ray within the cluster C_s^{SS}. Also, the delay, phase shift, and Doppler shift of NLoS component via the n_s-th ray within the cluster C_s^{SS} are given as

$$\tau_{qp,s,n_s}^{\text{SS}}(t)=\frac{\left\|\mathbf{D}_{p,s,n_s}^{\text{SS,T}}(t)\right\|+\left\|\mathbf{D}_{q,s,n_s}^{\text{SS,R}}(t)\right\|}{c} \tag{7}$$

$$\varphi_{qp,s,n_s}^{\text{SS}}(t)=\varphi_0+\frac{2\pi}{\lambda}\left[\left\|\mathbf{D}_{p,s,n_s}^{\text{SS,T}}(t)\right\|+\left\|\mathbf{D}_{q,s,n_s}^{\text{SS,R}}(t)\right\|\right] \tag{8}$$

$$f_{p/q,s,n_s}^{\text{SS,T/R}}(t)=\frac{1}{\lambda}\frac{\left\langle\mathbf{D}_{p/q,s,n_s}^{\text{SS,T/R}}(t),\mathbf{v}^{\text{T/R}}(t)\right\rangle}{\left\|\mathbf{D}_{p/q,s,n_s}^{\text{SS,T/R}}(t)\right\|} \tag{9}$$

where $\mathbf{D}_{p/q,s,n_s}^{\text{SS,T/R}}(t)$ is the distance vector between the n_s-th ray within the cluster C_s^{SS} and the antenna $\text{A}_{p/q}^{\text{T/R}}$. Furthermore, the distance vector $\mathbf{D}_{p,s,n_s}^{\text{SS,T}}(t)$ can be represented by

$$\mathbf{D}_{p,s,n_s}^{\text{SS,T}}(t)=\mathbf{D}_{s,n_s}^{\text{SS,T}}(0)-\int_0^t\mathbf{v}^{\text{T}}(t)\text{d}t-\mathbf{A}_p^{\text{T}} \tag{10}$$

where $\mathbf{A}_p^{\text{T}}$ is the vector of Tx antenna A_p^{T}. $\mathbf{D}_{s,n_s}^{\text{SS,T}}(0)$ is the distance vector between the n_s-th ray within the cluster C_s^{SS} and the Tx center at initial time and is given as

$$\mathbf{D}_{s,n_s}^{\text{SS,T}}(0)=\|\mathbf{D}_{s,n_s}^{\text{SS,T}}(0)\|\begin{bmatrix}\cos\alpha_{s,n_s}^{\text{SS,T}}(0)\cos\beta_{s,n_s}^{\text{SS,T}}(0)\\ \sin\alpha_{s,n_s}^{\text{SS,T}}(0)\cos\beta_{s,n_s}^{\text{SS,T}}(0)\\ \sin\beta_{s,n_s}^{\text{SS,T}}(0)\end{bmatrix} \tag{11}$$

where $\alpha_{s,n_s}^{\text{SS,T}}(0)$ and $\beta_{s,n_s}^{\text{SS,T}}(0)$ are the azimuth and elevation angles of the distance vector $\mathbf{D}_{s,n_s}^{\text{SS,T}}(0)$. Due to the single-bouncing propagation, the distance vectors $\mathbf{D}_{p,s,n_s}^{\text{SS,T}}(t)$ and

$\mathbf{D}^{\mathrm{SS,R}}_{q,s,n_s}(t)$ are correlated. Based on the geometrical relationship, the distance vector $\mathbf{D}^{\mathrm{SS,R}}_{q,s,n_s}(t)$ is computed as

$$\mathbf{D}^{\mathrm{SS,R}}_{q,s,n_s}(t) = \mathbf{D}^{\mathrm{SS,T}}_{p,s,n_s}(t) - \mathbf{D}^{\mathrm{LoS}}_{qp}(t). \tag{12}$$

2) Static Twin-Clusters: The complex channel gain of the sub-channel related to the Tx antenna $\mathrm{A}^{\mathrm{T}}_p$ and the Rx antenna $\mathrm{A}^{\mathrm{R}}_q$ via the n_i-th ray within the cluster $\mathrm{C}^{\mathrm{SM,T/R}}_i$ is given as

$$h^{\mathrm{SM}}_{qp,i,n_i}(t) = Q_{T_{\mathrm{E}}(t)}\sqrt{P^{\mathrm{SM}}_{i,n_i}(t)} \times \exp\left\{j2\pi\left[\int_0^t f^{\mathrm{SM,T}}_{p,i,n_i}(t)\mathrm{d}t + \int_0^t f^{\mathrm{SM,R}}_{q,i,n_i}(t)\mathrm{d}t\right] + j\varphi^{\mathrm{SM}}_{qp,i,n_i}(t)\right\} \tag{13}$$

where $P^{\mathrm{SM}}_{i,n_i}(t)$ is the power of the n_i-th ray within the cluster $\mathrm{C}^{\mathrm{SM,T/R}}_i$. Note that the phase shift and Doppler shift are derived similarly to the cluster $\mathrm{C}^{\mathrm{SS}}_s$ in (8) and (9) , and are written as $\varphi^{\mathrm{SM}}_{qp,i,n_i}(t) = \varphi_0 + \frac{2\pi}{\lambda}\left[\left\|\mathbf{D}^{\mathrm{SM,T}}_{p,i,n_i}(t)\right\| + \left\|\mathbf{D}^{\mathrm{SM,R}}_{q,i,n_i}(t)\right\| + c\tilde{\tau}^{\mathrm{SM}}_{qp,i,n_i}(t)\right]$ and $f^{\mathrm{SM,T/R}}_{p/q,i,n_i}(t) = \frac{1}{\lambda}\frac{\left\langle \mathbf{D}^{\mathrm{SM,T/R}}_{p/q,i,n_i}(t), \mathbf{v}^{\mathrm{T/R}}(t)\right\rangle}{\left\|\mathbf{D}^{\mathrm{SM,T/R}}_{p/q,i,n_i}(t)\right\|}$, respectively. However, unlike static single-cluster $\mathrm{C}^{\mathrm{SS}}_s$, the distance vectors $\mathbf{D}^{\mathrm{SM,T}}_{p,i,n_i}(t)$ and $\mathbf{D}^{\mathrm{SM,R}}_{q,i,n_i}(t)$ of static twin-clusters $\mathrm{C}^{\mathrm{SM,T/R}}_i$ are uncorrelated, which should be calculated separately. The calculation of distance vectors $\mathbf{D}^{\mathrm{SM,T}}_{p,i,n_i}(t)$ and $\mathbf{D}^{\mathrm{SM,R}}_{q,i,n_i}(t)$ is similar to that of the distance vector $\mathbf{D}^{\mathrm{SS,T}}_{p,s,n_s}(t)$ in (10) and (11). Furthermore, in the multi-bouncing propagation, the delay of virtual link between twin-clusters, named as the virtual delay, needs to be considered and the delay of NLoS component via the n_i-th ray within the cluster $\mathrm{C}^{\mathrm{SM,T/R}}_i$ is expressed as

$$\tau^{\mathrm{SM}}_{qp,i,n_i}(t) = \frac{\left\|\mathbf{D}^{\mathrm{SM,T}}_{p,i,n_i}(t)\right\| + \left\|\mathbf{D}^{\mathrm{SM,R}}_{q,i,n_i}(t)\right\|}{c} + \tilde{\tau}^{\mathrm{SM}}_{qp,i,n_i}(t) \tag{14}$$

where $\tilde{\tau}^{\mathrm{SM}}_{qp,i,n_i}(t)$ is the virtual delay of the twin-clusters $\mathrm{C}^{\mathrm{SM,T}}_i$ and $\mathrm{C}^{\mathrm{SM,R}}_i$ and follows the exponential distribution [25].

D. Complex Channel Gain of NLoS Component via Dynamic Single-Clusters and Twin-Clusters

Similar to static clusters, the complex channel gain of NLoS components via dynamic single/twin-clusters is obtained.

1) Dynamic Single-Clusters: The complex channel gain of the sub-channel related to the Tx and Rx antennas $\mathrm{A}^{\mathrm{T}}_p$ and $\mathrm{A}^{\mathrm{R}}_q$ via the n_d-th ray within the cluster $\mathrm{C}^{\mathrm{DS}}_d$ is written by

$$h^{\mathrm{DS}}_{qp,d,n_d}(t) = Q_{T_{\mathrm{E}}(t)}\sqrt{P^{\mathrm{DS}}_{d,n_d}(t)} \times \exp\left\{j2\pi\left[\int_0^t f^{\mathrm{DS,T}}_{p,d,n_d}(t)\mathrm{d}t + \int_0^t f^{\mathrm{DS,R}}_{q,d,n_d}(t)\mathrm{d}t\right] + j\varphi^{\mathrm{DS}}_{qp,d,n_d}(t)\right\} \tag{15}$$

where $P^{\mathrm{DS}}_{d,n_d}(t)$ is the power of the n_d-th ray within the cluster $\mathrm{C}^{\mathrm{DS}}_d$. Similar to the static single-cluster C^{SS}_s, the delay and phase shift of NLoS component via the dynamic single-cluster $\mathrm{C}^{\mathrm{DS}}_d$ are $\tau^{\mathrm{DS}}_{qp,d,n_d}(t) = \frac{\left\|\mathbf{D}^{\mathrm{DS,T}}_{p,d,n_d}(t)\right\| + \left\|\mathbf{D}^{\mathrm{DS,R}}_{q,d,n_d}(t)\right\|}{c}$ and $\varphi^{\mathrm{DS}}_{qp,d,n_d}(t) = \varphi_0 + \frac{2\pi}{\lambda}\left[\left\|\mathbf{D}^{\mathrm{DS,T}}_{p,d,n_d}(t)\right\| + \left\|\mathbf{D}^{\mathrm{DS,R}}_{q,d,n_d}(t)\right\|\right]$. Nonetheless, the Doppler shift of NLoS component via rays within dynamic clusters is different from that of NLoS component via rays within static clusters and is given as

$$f^{\mathrm{DS,T/R}}_{p/q,d,n_d}(t) = \frac{1}{\lambda}\frac{\left\langle \mathbf{D}^{\mathrm{DS,T/R}}_{p/q,d,n_d}(t), \mathbf{v}^{\mathrm{T/R}}(t) - \mathbf{v}^{\mathrm{DS}}_d(t)\right\rangle}{\left\|\mathbf{D}^{\mathrm{DS,T/R}}_{p/q,d,n_d}(t)\right\|} \tag{16}$$

where $\mathbf{D}^{\mathrm{DS,T/R}}_{p/q,d,n_d}(t)$ is the distance vector between the n_d-th ray within the cluster $\mathrm{C}^{\mathrm{DS}}_d$ and the antenna $\mathrm{A}^{\mathrm{T/R}}_{p/q}$. The distance vector $\mathbf{D}^{\mathrm{DS,T}}_{p,d,n_d}(t)$ is expressed as

$$\mathbf{D}^{\mathrm{DS,T}}_{p,d,n_d}(t) = \mathbf{D}^{\mathrm{DS,T}}_{d,n_d}(0) - \int_0^t \mathbf{v}^{\mathrm{T}}(t)\mathrm{d}t + \int_0^t \mathbf{v}^{\mathrm{DS}}_d(t)\mathrm{d}t - \mathbf{A}^{\mathrm{T}}_p \tag{17}$$

where $\mathbf{D}^{\mathrm{DS,T}}_{d,n_d}(0)$ is the distance vector between the n_d-th ray within the cluster $\mathrm{C}^{\mathrm{DS}}_d$ and the Tx center at initial time. Also, the distance vector $\mathbf{D}^{\mathrm{DS,R}}_{q,d,n_d}(t)$ can be calculated by $\mathbf{D}^{\mathrm{DS,R}}_{q,d,n_d}(t) = \mathbf{D}^{\mathrm{DS,T}}_{p,d,n_d}(t) - \mathbf{D}^{\mathrm{LoS}}_{qp}(t)$.

2) Dynamic Twin-Clusters: The complex channel gain of the sub-channel related to the Tx and Rx antennas $\mathrm{A}^{\mathrm{T}}_p$ and $\mathrm{A}^{\mathrm{R}}_q$ via the n_j-th ray within the cluster $\mathrm{C}^{\mathrm{DM,T/R}}_j$ is given by

$$h^{\mathrm{DM}}_{qp,j,n_j}(t) = Q_{T_{\mathrm{E}}(t)}\sqrt{P^{\mathrm{DM}}_{j,n_j}(t)} \times \exp\left\{j2\pi\left[\int_0^t f^{\mathrm{DM,T}}_{p,j,n_j}(t)\mathrm{d}t + \int_0^t f^{\mathrm{DM}}_{q,j,n_j}(t)\mathrm{d}t\right] + j\varphi^{\mathrm{DM}}_{qp,j,n_j}(t)\right\} \tag{18}$$

where $P^{\mathrm{DM}}_{j,n_j}(t)$ is the power of the n_j-th ray within the cluster $\mathrm{C}^{\mathrm{DM,T/R}}_j$. Based on the aforementioned analysis, the delay, phase shift, and Doppler shift of the NLoS component via the n_j-th ray within the cluster $\mathrm{C}^{\mathrm{DM,T/R}}_j$ are analogously computed by $\tau^{\mathrm{DM}}_{qp,j,n_j}(t) = \frac{\left\|\mathbf{D}^{\mathrm{DM,T}}_{p,j,n_j}(t)\right\| + \left\|\mathbf{D}^{\mathrm{DM,R}}_{q,j,n_j}(t)\right\|}{c} + \tilde{\tau}^{\mathrm{DM}}_{qp,j,n_j}(t)$, $\varphi^{\mathrm{DM}}_{qp,j,n_j}(t) = \varphi_0 + \frac{2\pi}{\lambda}\left[\left\|\mathbf{D}^{\mathrm{DM,T}}_{p,j,n_j}(t)\right\| + \left\|\mathbf{D}^{\mathrm{DM,R}}_{q,j,n_j}(t)\right\| + c\tilde{\tau}^{\mathrm{DM}}_{qp,j,n_j}(t)\right]$, and $f^{\mathrm{DM,T/R}}_{p/q,j,n_j}(t) = \frac{1}{\lambda}\frac{\left\langle \mathbf{D}^{\mathrm{DM,T/R}}_{p/q,j,n_j}(t), \mathbf{v}^{\mathrm{T/R}}(t) - \mathbf{v}^{\mathrm{DM,T/R}}_j(t)\right\rangle}{\left\|\mathbf{D}^{\mathrm{DM,T/R}}_{p/q,j,n_j}(t)\right\|}$. Based on the geometry relationship, transmission paths of antennas and rays within clusters are computed, where the different angular parameters of transmission paths are imitated. Hence, the spherical wavefront propagation in massive MIMO channels is mimicked sufficiently.

The channel impulse response (CIR) of the developed IS-GBSM with delay τ at time t can be represented as a matrix $\mathbf{H}(t,\tau) = [h_{qp}(t,\tau)]_{M_{\mathrm{R}}\times M_{\mathrm{T}}}$ with $q = 1, 2, ..., M_{\mathrm{R}}$ and $p = 1, 2, ..., M_{\mathrm{T}}$. $\mathbf{H}(t,\tau)$ contains the LoS, GR, as well as NLoS components. The CIR $h_{qp}(t,\tau)$ related to the Tx and Rx antenna element pair p and q can be expressed as (19), shown at the top of the next page, where $K(t)$ denotes the Ricean factor. $\eta^{\mathrm{GR}}(t)$, $\eta^{\mathrm{SS}}(t)$, $\eta^{\mathrm{SM}}(t)$, $\eta^{\mathrm{DS}}(t)$, and $\eta^{\mathrm{DM}}(t)$ represent the power proportions of the GR component, component via static single-cluster, component via static twin-cluster, component via dynamic single-cluster, and component via dynamic twin-cluster. These power proportions have $\eta^{\mathrm{GR}}(t)+\eta^{\mathrm{SS}}(t)+\eta^{\mathrm{SM}}(t)+\eta^{\mathrm{DS}}(t)+\eta^{\mathrm{DM}}(t) = 1$. Finally, it is noteworthy that the integration of time and time-variant acceleration are essential for the capturing of continuously arbitrary VMTs, where the numerical calculation of the integral can be efficiently computed by the method of superposition calculation. As a result, by modeling continuously arbitrary VMTs, it is possible to acquire the CIR and investigate channel properties under all positions on the track.

$$
\begin{aligned}
h_{qp}(t,\tau) = & \underbrace{\sqrt{\frac{K(t)}{K(t)+1}} h_{qp}^{\mathrm{LoS}}(t)\delta\left(\tau-\tau_{qp}^{\mathrm{LoS}}(t)\right)}_{\text{LoS Component}} + \underbrace{\sqrt{\frac{\eta^{\mathrm{GR}}(t)}{K(t)+1}} h_{qp}^{\mathrm{GR}}(t)\delta\left(\tau-\tau_{qp}^{\mathrm{GR}}(t)\right)}_{\text{GR Component}} \\
& + \underbrace{\sqrt{\frac{\eta^{\mathrm{SS}}(t)}{K(t)+1}} \sum_{s=1}^{S(t)} \sum_{n_s=1}^{N_s(t)} h_{qp,s,n_s}^{\mathrm{SS}}(t)\delta\left(\tau-\tau_{qp,s,n_s}^{\mathrm{SS}}(t)\right) + \sqrt{\frac{\eta^{\mathrm{DS}}(t)}{K(t)+1}} \sum_{d=1}^{D(t)} \sum_{n_d=1}^{N_d(t)} h_{qp,d,n_d}^{\mathrm{DS}}(t)\delta\left(\tau-\tau_{qp,d,n_d}^{\mathrm{DS}}(t)\right)}_{\text{NLoS Component via Single-Clusters}} \\
& + \underbrace{\sqrt{\frac{\eta^{\mathrm{SM}}(t)}{K(t)+1}} \sum_{i=1}^{I(t)} \sum_{n_i=1}^{N_i(t)} h_{qp,i,n_i}^{\mathrm{SM}}(t)\delta\left(\tau-\tau_{qp,i,n_i}^{\mathrm{SM}}(t)\right) + \sqrt{\frac{\eta^{\mathrm{DM}}(t)}{K(t)+1}} \sum_{j=1}^{J(t)} \sum_{n_j=1}^{N_j(t)} h_{qp,j,n_j}^{\mathrm{DM}}(t)\delta\left(\tau-\tau_{qp,j,n_j}^{\mathrm{DM}}(t)\right)}_{\text{NLoS Component via Twin-Clusters}}
\end{aligned} \tag{19}
$$

III. A New S-T-F Non-Stationarity of V2V Channels with T-S Consistency Modeling Method

In the upcoming 6G, S-T-F non-stationarity of V2V channels with T-S consistency needs to be modeled. In V2V communication scenarios, it is necessary to consider the effects of mixed-bouncing propagation, i.e., single/twin-clusters, VTD, i.e., static/dynamic clusters, and continuously arbitrary VMTs. In this section, a new method, named as the S-T-F non-stationarity of V2V channels with T-S consistency modeling method, is developed, which can model S-T-F non-stationarity with T-S consistency in consideration of mixed-bouncing propagation, VTD, and continuously arbitrary VMTs.

A. Modeling of Space Non-Stationarity and Consistency by Observable Semi-Spheres Assigned to Antennas

For channel models in [26], [27], the visibility region method is employed to model channel non-stationarity. In the visibility region method, only clusters in the visibility region are observable clusters. Since the models in [26], [27] are two-dimensional (2D), the visibility region is modeled as circles. Nonetheless, in the three-dimensional (3D) channel model, the visibility region needs to be modeled as spheres instead of circles. Further considering that vehicles move on the 2D ground, the visibility region is modeled as semi-spheres in the proposed 3D V2V channel model. The semi-sphere is constructed with each antenna as the center. By developing observable semi-spheres, different antennas with different observable semi-spheres have different sets of array observable clusters, hence modeling space non-stationarity. For adjacent antennas, they share many clusters, namely the shared array observable clusters, as their observable semi-spheres have the overlap area, thus capturing space consistency. To avoid the repetition, the Tx side is taken as an instance for analysis and the Rx side follows the same procedure.

The number of shared array observable clusters strongly depends on the overlap area. The overlap area of observable semi-spheres of two adjacent antennas A_p^{T} and A_{p+1}^{T} with spacing δ_{T} is a spherical crown, whose volume $V_{\mathrm{share}}^{\mathrm{T}}$ can be calculated based on [18]

$$
V_{\mathrm{share}}^{\mathrm{T}} = \frac{\pi\left(16{r_{\mathrm{a}}^{\mathrm{T}}}^3 - 12{r_{\mathrm{a}}^{\mathrm{T}}}^2\delta_{\mathrm{T}} + \delta_{\mathrm{T}}^3\right)}{24} \tag{20}
$$

where $r_{\mathrm{a}}^{\mathrm{T}}$ denotes the radius of observable semi-sphere. At the Tx side, since antennas are uniformly distributed on the array with spacing δ_{T}, the radius $r_{\mathrm{a}}^{\mathrm{T}}$ of each observable semi-sphere is the same. To quantitatively calculate the radius $r_{\mathrm{a}}^{\mathrm{T}}$, a novel parameter $\Gamma_{\mathrm{space}}^{\mathrm{T}}$ is given, which represents the ratio of volume $V_{\mathrm{share}}^{\mathrm{T}}$ of overlap area to volume $V_{\mathrm{space}}^{\mathrm{T}}$ of observable semi-sphere

$$
\Gamma_{\mathrm{space}}^{\mathrm{T}} = \frac{V_{\mathrm{share}}^{\mathrm{T}}}{V_{\mathrm{space}}^{\mathrm{T}}} = \frac{V_{\mathrm{space}}^{\mathrm{T}}}{\frac{2}{3}\pi{r_{\mathrm{a}}^{\mathrm{T}}}^3} = \frac{16{r_{\mathrm{a}}^{\mathrm{T}}}^3 - 12{r_{\mathrm{a}}^{\mathrm{T}}}^2\delta_{\mathrm{T}} + \delta_{\mathrm{T}}^3}{16{r_{\mathrm{a}}^{\mathrm{T}}}^3}. \tag{21}
$$

Clusters in the observable semi-sphere are array observable clusters and only clusters in the overlap area are shared array observable clusters. Assumed that clusters are uniformly distributed in the environment. Hence, the parameter $\Gamma_{\mathrm{space}}^{\mathrm{T}}$ describes the probability that an array observable cluster is a shared array observable cluster, which is simultaneously observable to an antenna A_p^{T} and its adjacent antenna A_{p+1}^{T}. In the cluster array evolution, the parameter $\Gamma_{\mathrm{space}}^{\mathrm{T}}$ also represents the *probability* that a surviving cluster for an antenna A_p^{T} is still surviving when it evolves to the adjacent antenna A_{p+1}^{T}. This is consistent with the spatial survival probability. The spatial survival probability at Tx is given by [28]

$$
P_{\mathrm{survival}}^{\mathrm{T}} = \exp\left(\frac{-\lambda_{\mathrm{R}}\delta_{\mathrm{T}}}{D_{\mathrm{c}}^{\mathrm{a}}}\right) \tag{22}
$$

where λ_{R} is the recombination rate and $D_{\mathrm{c}}^{\mathrm{a}}$ denotes the scenario-dependent correlation factor on the array axis. Make the parameter $\Gamma_{\mathrm{space}}^{\mathrm{T}}$ and spatial survival probability $P_{\mathrm{survival}}^{\mathrm{T}}$ equal, i.e., $\Gamma_{\mathrm{space}}^{\mathrm{T}} = P_{\mathrm{survival}}^{\mathrm{T}}$ to solve for the radius $r_{\mathrm{a}}^{\mathrm{T}}$

$$
\frac{16{r_{\mathrm{a}}^{\mathrm{T}}}^3 - 12{r_{\mathrm{a}}^{\mathrm{T}}}^2\delta_{\mathrm{T}} + \delta_{\mathrm{T}}^3}{16{r_{\mathrm{a}}^{\mathrm{T}}}^3} = \exp\left(\frac{-\lambda_{\mathrm{R}}\delta_{\mathrm{T}}}{D_{\mathrm{c}}^{\mathrm{a}}}\right). \tag{23}
$$

Based on the Cardano formula, the radius $r_{\mathrm{a}}^{\mathrm{T}}$ is given by

$$
r_{\mathrm{a}}^{\mathrm{T}} = \left\{ \sqrt[3]{\xi_{\mathrm{space}}^{\mathrm{T}} + \sigma_{\mathrm{space}}^{\mathrm{T}}} + \sqrt[3]{\xi_{\mathrm{space}}^{\mathrm{T}} - \sigma_{\mathrm{space}}^{\mathrm{T}}} + \frac{1}{4\left[1-\exp\left(\frac{-\lambda_{\mathrm{R}}\delta_{\mathrm{T}}}{D_{\mathrm{c}}^{\mathrm{a}}}\right)\right]} \right\}\delta_{\mathrm{T}} \tag{24}
$$

where $\xi_{\mathrm{space}}^{\mathrm{T}}$ and $\sigma_{\mathrm{space}}^{\mathrm{T}}$ are respectively written as

$$
\xi_{\mathrm{space}}^{\mathrm{T}} = \frac{-2\left[1-\exp\left(\frac{-\lambda_{\mathrm{R}}\delta_{\mathrm{T}}}{D_{\mathrm{c}}^{\mathrm{a}}}\right)\right]^2 + 1}{64\left[1-\exp\left(\frac{-\lambda_{\mathrm{R}}\delta_{\mathrm{T}}}{D_{\mathrm{c}}^{\mathrm{a}}}\right)\right]^3} \tag{25}
$$

$$\sigma_{\text{space}}^{\text{T}}=\sqrt{\frac{\left[1-\exp\left(\frac{-\lambda_{\text{R}}\delta_{\text{T}}}{D_{\text{c}}^{\text{a}}}\right)\right]^{2}-1}{1024\left[1-\exp\left(\frac{-\lambda_{\text{R}}\delta_{\text{T}}}{D_{\text{c}}^{\text{a}}}\right)\right]^{4}}}. \tag{26}$$

With the help of the derived closed-form solution, the impacts of the recombination rate λ_{R}, adjacent antenna spacing δ_{T}, and scenario-dependent correlation factor D_{c}^{a} on the radius r_{a}^{T} can be investigated. By properly adjusting the recombination rate λ_{R} and factor D_{c}^{a}, the developed visibility region method in the space domain can be applied to a variety of scenarios.

1) Conditions of Array Observable Static/Dynamic Single-Clusters: In the proposed mmWave V2V model, the adjacent antenna spacing is small. According to (24), the radius r_{a}^{T} is proportional to the adjacent antenna spacing δ_{T}, which leads to the small radius r_{a}^{T}. Consequently, it is necessary to introduce parameters, namely shrinkage factors on the array axis, which can shrink the distance from the antenna A_p^{T} to the cluster. Specifically, the distances between static/dynamic single-clusters and the antenna A_p^{T} are shrunk by the shrinkage factors $\varepsilon_{\text{space}}^{\text{SS,T}}$ and $\varepsilon_{\text{space}}^{\text{DS,T}}$ and can be given by $\tilde{D}_{p,s}^{\text{SS,T}}(t)=\frac{D_{p,s}^{\text{SS,T}}(t)}{\varepsilon_{\text{space}}^{\text{SS,T}}}$ and $\tilde{D}_{p,d}^{\text{DS,T}}(t)=\frac{D_{p,d}^{\text{DS,T}}(t)}{\varepsilon_{\text{space}}^{\text{DS,T}}}$. Based on the shrinkage distance and radius r_{a}^{T}, the clusters C_s^{SS} and C_d^{DS} are observable to the Tx antenna A_p^{T} that need to satisfy $\tilde{D}_{p,s}^{\text{SS,T}}(t)<r_{\text{a}}^{\text{T}}$ and $\tilde{D}_{p,d}^{\text{DS,T}}(t)<r_{\text{a}}^{\text{T}}$, respectively. Obviously, the values of shrinkage factors have great impacts on the array observable cluster condition. To properly set the value of shrinkage factors, randomly select a Tx antenna, e.g., the antenna A_p^{T}, assuming that it can observe all static/dynamic single-clusters at initial time t_0. This assumption is consistent with the standardized channel model in [29]. Under this assumption, shrinkage factors $\varepsilon_{\text{space}}^{\text{SS,T}}$ and $\varepsilon_{\text{space}}^{\text{DS,T}}$ are given by

$$\varepsilon_{\text{space}}^{\text{SS,T}}=\max\left\{\frac{D_{p,s}^{\text{SS,T}}(t_0)}{r_{\text{a}}^{\text{T}}}\right\},p=1,2,\cdots,M_{\text{T}},s=1,2,\cdots,S\left(t_0\right) \tag{27}$$

$$\varepsilon_{\text{space}}^{\text{DS,T}}=\max\left\{\frac{D_{p,d}^{\text{DS,T}}(t_0)}{r_{\text{a}}^{\text{T}}}\right\},p=1,2,\cdots,M_{\text{T}},d=1,2,\cdots,D\left(t_0\right). \tag{28}$$

Note that, the conditions of the array observable static and dynamic single-clusters C_s^{SS} and C_d^{DS} are that clusters C_s^{SS} and C_d^{DS} are observable to both the antenna A_p^{T} and the Rx antenna A_q^{R}, i.e., $\tilde{D}_{p,s}^{\text{SS,T}}(t)<r_{\text{a}}^{\text{T}},\tilde{D}_{q,s}^{\text{SS,R}}(t)<r_{\text{a}}^{\text{R}}$ and $\tilde{D}_{p,d}^{\text{DS,T}}(t)<r_{\text{a}}^{\text{T}},\tilde{D}_{q,d}^{\text{DS,R}}(t)<r_{\text{a}}^{\text{R}}$, respectively.

2) Conditions of Array Observable Static/Dynamic Twin-Clusters: Analogous to single-clusters, the distances between static/dynamic twin-clusters nearby Tx and antenna A_p^{T} are shrunk by the shrinkage factors $\varepsilon_{\text{space}}^{\text{SM,T}}$ and $\varepsilon_{\text{space}}^{\text{DM,T}}$. The corresponding shrinkage distances are $\tilde{D}_{p,i}^{\text{SM,T}}(t)=\frac{D_{p,i}^{\text{SM,T}}(t)}{\varepsilon_{\text{space}}^{\text{SM,T}}}$ and $\tilde{D}_{p,j}^{\text{DM,T}}(t)=\frac{D_{p,j}^{\text{DM,T}}(t)}{\varepsilon_{\text{space}}^{\text{DM,T}}}$. The twin-clusters nearby Tx $C_i^{\text{SM,T}}$ and $C_j^{\text{DM,T}}$ observable to the Tx antenna A_p^{T} have $\tilde{D}_{p,i}^{\text{SM,T}}(t)<r_{\text{a}}^{\text{T}}$ and $\tilde{D}_{p,j}^{\text{DM,T}}(t)<r_{\text{a}}^{\text{T}}$. Further assume that a randomly selected Tx antenna, e.g., A_p^{T}, can observe all static/dynamic twin-clusters nearby Tx at initial time t_0, and thus the shrinkage factors $\varepsilon_{\text{space}}^{\text{SM,T}}$ and $\varepsilon_{\text{space}}^{\text{DM,T}}$ are given by

$$\varepsilon_{\text{space}}^{\text{SM,T}}=\max\left\{\frac{D_{p,i}^{\text{SM,T}}(t_0)}{r_{\text{a}}^{\text{T}}}\right\},p=1,2,\cdots,M_{\text{T}},i=1,2,\cdots,I\left(t_0\right) \tag{29}$$

$$\varepsilon_{\text{space}}^{\text{DM,T}}=\max\left\{\frac{D_{p,j}^{\text{DM,R}}(t_0)}{r_{\text{a}}^{\text{T}}}\right\},p=1,2,\cdots,M_{\text{T}},j=1,2,\cdots,J\left(t_0\right). \tag{30}$$

Unlike single-clusters, the twin-clusters nearby Tx observable to the Tx antenna A_p^{T} and the twin-clusters nearby Rx observable to the Rx antenna A_q^{R} need to be randomly paired. Only successfully paired static/dynamic twin-clusters nearby Tx and Rx, e.g., $C_i^{\text{SM,T}}/C_j^{\text{DM,T}}$ and $C_i^{\text{SM,R}}/C_j^{\text{DM,R}}$, will form array observable static/dynamic twin-clusters. Therefore, the conditions of array observable static/dynamic twin-clusters are that clusters $C_i^{\text{SM,T}}/C_j^{\text{DM,T}}$ and $C_i^{\text{SM,R}}/C_j^{\text{DM,R}}$ are observable to the Tx antenna A_p^{T} and the Rx antenna A_q^{R}, respectively, and then clusters $C_i^{\text{SM,T}}/C_j^{\text{DM,T}}$ and $C_i^{\text{SM,R}}/C_j^{\text{DM,R}}$ are paired.

B. Modeling of Time Non-Stationarity and Consistency by Observable Spheres Assigned to Clusters

To mimic time non-stationarity and consistency, the visibility region method in the time domain is developed. Unlike the 2D general COST 2100 channel model [21] that defined the visibility region as circles, the proposed model is 3D and further distinguishes static/dynamic single/twin-clusters. These clusters are distributed in 3D space, not limited to 2D ground. In this case, the visibility region in the proposed model is characterized as the sphere with each static/dynamic single/twin-cluster as the center. When the center of the transceiver antenna array is in a sphere of a static/dynamic single/twin-cluster at time t, the static/dynamic single/twin-cluster is observable to this time t. With the help of observable spheres, as the transceiver and dynamic cluster move, time observable cluster sets change over time, thus modeling time non-stationarity. Owing to their smooth and continuous movements, adjacent moments share many identical time observable clusters, thus capturing time consistency. Also, take the Tx side as an example for analysis.

1) Conditions of Time Observable Static Single/Twin-Clusters: The velocity vectors of static single-cluster C_s^{SS} and twin-cluster nearby Tx $C_i^{\text{SM,T}}$ relative to the Tx array are $\mathbf{v}\text{'}_s^{\text{SS}}(t)=\mathbf{v}\text{'}_s^{\text{SM,T}}(t)=-\mathbf{v}^{\text{T}}(t)$. The Tx array can be regarded as static for the cluster $C_s^{\text{SS}}/C_i^{\text{SM,T}}$. As the cluster $C_s^{\text{SS}}/C_i^{\text{SM,T}}$ moves relative to the Tx array with the velocity vector $\mathbf{v}\text{'}_s^{\text{SS}}(t)/\mathbf{v}\text{'}_i^{\text{SM,T}}(t)$, its observable sphere also moves. At two adjacent moments t and $t+\Delta t$, its observable sphere has the overlap area, which is dependable on the *relative movement distance* $D_s^{\text{SS,T}}(t)/D_i^{\text{SM,T}}(t)$ between this cluster $C_s^{\text{SS}}/C_i^{\text{SM,T}}$ and Tx array in a time interval Δt. Distance parameters $D_s^{\text{SS,T}}(t)$ and $D_i^{\text{SM,T}}(t)$ are equal, which are unified as

$$D^{\text{S,T}}(t)=D_s^{\text{SS,T}}(t)=D_i^{\text{SM,T}}(t)=\int_t^{t+\Delta t}\left\|-\mathbf{v}^{\text{T}}(t)\right\|\mathrm{d}t. \tag{31}$$

The time interval Δt is short in mmWave high-mobility V2V communications, where channels need to be updated frequently. The distance parameter $D^{\text{S,T}}(t)$ can be approximated to be equal at two adjacent moments t and $t+\Delta t$.

Consequently, the overlap area of observable spheres assigned to static clusters can be regarded as consisting of two identical spherical crowns, whose volume $V_{\text{share}}^{\text{S,T}}(t)$ is computed similarly to the volume $V_{\text{share}}^{\text{T}}$ in (20) and is expressed by

$$V_{\text{share}}^{\text{S,T}}(t)=\frac{\pi\left[16{r_{\text{t}}^{\text{S,T}}}^3(t)-12{r_{\text{t}}^{\text{S,T}}}^2(t)D^{\text{S,T}}(t)+{D^{\text{S,T}}}^3(t)\right]}{12} \tag{32}$$

where $r_{\text{t}}^{\text{S,T}}(t)$ denotes the time-variant radius of Tx observable sphere assigned to the static cluster. Similarly, a new parameter $\Gamma_{\text{time}}^{\text{S,T}}(t)$ is developed to denote the ratio of volume of overlap area to the volume of observable sphere and is given as

$$\Gamma_{\text{time}}^{\text{S,T}}(t)=\frac{V_{\text{share}}^{\text{S,T}}(t)}{V_{\text{time}}^{\text{S,T}}(t)}=\frac{16{r_{\text{t}}^{\text{S,T}}}^3(t)-12{r_{\text{t}}^{\text{S,T}}}^2(t)D^{\text{S,T}}(t)+{D^{\text{S,T}}}^3(t)}{16{r_{\text{t}}^{\text{S,T}}}^3(t)}. \tag{33}$$

Only when the center of array is located in an observable sphere of a cluster at two adjacent moments simultaneously, the cluster is a shared time observable cluster. As the parameter $\Gamma_{\text{time}}^{\text{S,T}}(t)$ represents the *proportion* of overlap area in the observable sphere, it also characterizes the *probability* that an observable cluster at time t will still be observable at the next time instant $t+\Delta t$. This is in agreement with the definition of time survival probability in the birth-death process method from the perspective of cluster time evolution [29]. The time survival probability at Tx of static clusters is written as

$$P_{\text{survival}}^{\text{S,T}}(t)=\exp\left[\frac{-\lambda_{\text{R}}\int_t^{t+\Delta t}\left\|\mathbf{v}^{\text{T}}(t)\right\|\text{d}t}{D_{\text{c}}^{\text{t}}}\right] \tag{34}$$

where D_{c}^{t} denotes the scenario-dependent correlation factor on the time axis. Make the proportion of overlap area equal to the time survival probability, i.e., $\Gamma_{\text{time}}^{\text{S,T}}(t)=P_{\text{survival}}^{\text{S,T}}(t)$. Similarly, the radius of observable spheres assigned to static clusters is calculated as (35)–(37), shown at the top of the next page. The radius $r_{\text{t}}^{\text{S,T}}(t)$ is proportional to distance parameter $D^{\text{S,T}}(t)$ and the effects of recombination rate λ_{R} and velocity vector of Tx array $\mathbf{v}^{\text{T}}(t)$ on the radius $r_{\text{t}}^{\text{S,T}}(t)$ are explored. Note that the developed visibility region method in the time domain can support diverse scenarios by properly setting the recombination rate λ_{R} and factor D_{c}^{t}.

The small time interval Δt in mmWave V2V channels also results in the small radius $r_{\text{t}}^{\text{SS,T}}(t)$ of observable spheres based on (35)–(37). Similar to the array axis, shrinkage factors on the time axis $\varepsilon_{\text{time}}^{\text{SS,T}}$ and $\varepsilon_{\text{time}}^{\text{SM,T}}$ are introduced, which can shrink the distance from the center of Tx array to the static clusters C_s^{SS} and $C_i^{\text{SM,T}}$ at time t, i.e., $\tilde{D}_{Os}^{\text{SS,T}}(t)=\frac{D_{Os}^{\text{SS,T}}(t)}{\varepsilon_{\text{time}}^{\text{SS,T}}}$ and $\tilde{D}_{Oi}^{\text{SM,T}}(t)=\frac{D_{Oi}^{\text{SM,T}}(t)}{\varepsilon_{\text{time}}^{\text{SM,T}}}$. The *time observable static single/twin-cluster conditions at Tx*, i.e., static clusters C_s^{SS} and $C_i^{\text{SM,T}}$ are time observable clusters, are $\tilde{D}_{Os}^{\text{SS,T}}(t)<r_{\text{t}}^{\text{S,T}}(t)$ and $\tilde{D}_{Oi}^{\text{SM,T}}(t)<r_{\text{t}}^{\text{S,T}}(t)$. Also, the proper setting of shrinkage factors $\varepsilon_{\text{time}}^{\text{SS,T}}$ and $\varepsilon_{\text{time}}^{\text{SM,T}}$ is crucial. Similar to [28], assuming that all clusters are observable at initial time t_0 and the shrinkage factors $\varepsilon_{\text{time}}^{\text{SS,T}}$ and $\varepsilon_{\text{time}}^{\text{SM,T}}$ are determined by

$$\varepsilon_{\text{time}}^{\text{SS,T}}=\max\left\{\frac{D_{Os}^{\text{SS,T}}(t_0)}{r_{\text{t}}^{\text{S,T}}(t_0)}\right\},s=1,2,3,\cdots,S\left(t_0\right) \tag{38}$$

$$\varepsilon_{\text{time}}^{\text{SM,T}}=\max\left\{\frac{D_{Oi}^{\text{SM,T}}(t_0)}{r_{\text{t}}^{\text{S,T}}(t_0)}\right\},i=1,2,3,\cdots,I\left(t_0\right). \tag{39}$$

The condition of the time observable static single-cluster is that the cluster C_s^{SS} simultaneously satisfies $\tilde{D}_{Os}^{\text{SS,T}}(t)<r_{\text{t}}^{\text{S,T}}(t)$ and $\tilde{D}_{Os}^{\text{SS,R}}(t)<r_{\text{t}}^{\text{S,R}}(t)$. Unlike static single-clusters, the static twin-clusters nearby Tx $C_i^{\text{SM,T}}$ and Rx $C_i^{\text{SM,R}}$ need to meet $\tilde{D}_{Oi}^{\text{SM,T}}(t)<r_{\text{t}}^{\text{S,T}}(t)$ and $\tilde{D}_{Oi}^{\text{SM,R}}(t)<r_{\text{t}}^{\text{S,R}}(t)$, respectively. Only when they are paired can they form time observable static twin-clusters.

2) Conditions of Time Observable Dynamic Single/Twin-Clusters: The velocity vectors of dynamic single-cluster C_d^{DS} and twin-cluster nearby Tx $C_j^{\text{DM,T}}$ relative to the Tx array are $\mathbf{v}\text{'}_d^{\text{DS}}(t)=\mathbf{v}_d^{\text{DS}}(t)-\mathbf{v}^{\text{T}}(t)$ and $\mathbf{v}\text{'}_j^{\text{DM,T}}(t)=\mathbf{v}_j^{\text{DM,T}}(t)-\mathbf{v}^{\text{T}}(t)$, respectively. The observable sphere of the dynamic cluster C_d^{DS}/$C_j^{\text{DM,T}}$ at two adjacent moments t and $t+\Delta t$ has the overlap area, which also depends on the relative movement distance $D_d^{\text{DS,T}}(t)$/$D_j^{\text{DM,T}}(t)$ between the cluster C_d^{DS}/$C_j^{\text{DM,T}}$ and Tx array in a time interval Δt. The distance parameters $D_d^{\text{DS,T}}(t)$ and $D_j^{\text{DM,T}}(t)$ can be written as

$$D_{d/j}^{\text{DS/DM,T}}(t)=\int_t^{t+\Delta t}\left\|\mathbf{v}_{d/j}^{\text{DS/DM}}(t)-\mathbf{v}^{\text{T}}(t)\right\|\text{d}t. \tag{40}$$

By considering the multi-velocity of dynamic clusters, the relative distances $D_d^{\text{DS,T}}(t)$ and $D_j^{\text{DM,T}}(t)$ for different dynamic clusters are different. Similarly, the volume $V_{\text{share},d}^{\text{DS,T}}(t)$/$V_{\text{share},j}^{\text{DM,T}}(t)$ of overlap area of observable sphere assigned to the dynamic cluster C_d^{DS}/$C_j^{\text{DM,T}}$ can be obtained. Also, a new parameter $\Gamma_{\text{time}}^{\text{DS,T}}(t)$/$\Gamma_{\text{time}}^{\text{DM,T}}(t)$ is introduced to represent the ratio of volume of overlap area to the volume of observable sphere assigned to the cluster C_d^{DS}/$C_j^{\text{DM,T}}$

$$\begin{aligned}&\Gamma_{\text{time},d/j}^{\text{DS/DM,T}}(t)\\&=\frac{16{r_{\text{t},d/j}^{\text{DS/DM,T}}}^3(t)-12{r_{\text{t},d/j}^{\text{DS/DM}}}^2(t)D_{d/j}^{\text{DS/DM,T}}(t)+{D_{d/j}^{\text{DS/DM,T}}}^3(t)}{16{r_{\text{t},d/j}^{\text{DS/DM,T}}}^3(t)}\end{aligned} \tag{41}$$

where $r_{\text{t},d}^{\text{DS,T}}(t)$/$r_{\text{t},j}^{\text{DM,T}}(t)$ represents the time-varying radius of Tx observable sphere of the cluster C_d^{DS}/$C_j^{\text{DM,T}}$. Analogously, combined with the birth-death process, the time survival probabilities at Tx of dynamic clusters C_d^{DS} and $C_j^{\text{DM,T}}$ are given as

$$P_{\text{survival},d/j}^{\text{DS/DM,T}}(t)=\exp\left[\frac{-\lambda_{\text{R}}\int_t^{t+\Delta t}\left\|\mathbf{v}_{d/j}^{\text{DS/DM,T}}(t)-\mathbf{v}^{\text{T}}(t)\right\|\text{d}t}{D_{\text{c}}^{\text{t}}}\right]. \tag{42}$$

Make the proportion of overlap area and the time survival probability equal, i.e., $\Gamma_{\text{time},d}^{\text{DS,T}}(t)=P_{\text{survival},d}^{\text{DS,T}}(t)$ and $\Gamma_{\text{time},j}^{\text{DM,T}}(t)=P_{\text{survival},j}^{\text{DM,T}}(t)$, to solve the radius, which is given by (43)–(45), shown at the top of the next page. The radii of observable spheres assigned to different dynamic clusters are different due to the multi-velocity of dynamic clusters. For dynamic clusters, shrinkage factors on the time axis $\varepsilon_{\text{time}}^{\text{DS,T}}$ and $\varepsilon_{\text{time}}^{\text{DM,T}}$ are introduced and $\tilde{D}_{Od}^{\text{DS,T}}(t)=\frac{D_{Od}^{\text{DS,T}}(t)}{\varepsilon_{\text{time}}^{\text{DS,T}}}$ and $\tilde{D}_{Oj}^{\text{DM,T}}(t)=\frac{D_{Oj}^{\text{DM,T}}(t)}{\varepsilon_{\text{time}}^{\text{DM,T}}}$. The conditions that dynamic clusters C_d^{DS} and $C_j^{\text{DM,T}}$ are time observable clusters are $\tilde{D}_{Od}^{\text{DS,T}}(t)<r_{\text{t}}^{\text{DS,T}}(t)$ and $\tilde{D}_{Oj}^{\text{DM,T}}(t)<r_{\text{t}}^{\text{DM,T}}(t)$. Assuming

$$r_{\mathrm{t}}^{\mathrm{S,T}}(t)=\left\{\sqrt[3]{\xi_{\mathrm{time}}^{\mathrm{S,T}}(t)+\sigma_{\mathrm{time}}^{\mathrm{S,T}}(t)}+\sqrt[3]{\xi_{\mathrm{time}}^{\mathrm{S,T}}(t)-\sigma_{\mathrm{time}}^{\mathrm{S,T}}(t)}+\frac{1}{4\left\{1-\exp\left[\frac{-\lambda_{\mathrm{R}}\int_t^{t+\Delta t}\left\|\mathbf{v}^{\mathrm{T}}(t)\right\|\mathrm{d}t}{D_{\mathrm{c}}^{\mathrm{t}}}\right]\right\}}\right\}\int_t^{t+\Delta t}\left\|\mathbf{v}^{\mathrm{T}}(t)\right\|\mathrm{d}t \tag{35}$$

with

$$\xi_{\mathrm{time}}^{\mathrm{S,T}}(t)=\frac{-2\left\{1-\exp\left[\frac{-\lambda_{\mathrm{R}}\int_t^{t+\Delta t}\left\|\mathbf{v}^{\mathrm{T}}(t)\right\|\mathrm{d}t}{D_{\mathrm{c}}^{\mathrm{t}}}\right]\right\}^2+1}{64\left\{1-\exp\left[\frac{-\lambda_{\mathrm{R}}\int_t^{t+\Delta t}\left\|\mathbf{v}^{\mathrm{T}}(t)\right\|\mathrm{d}t}{D_{\mathrm{c}}^{\mathrm{t}}}\right]\right\}^3} \tag{36}$$

$$\sigma_{\mathrm{time}}^{\mathrm{S,T}}(t)=\sqrt{\frac{\left\{1-\exp\left[\frac{-\lambda_{\mathrm{R}}\int_t^{t+\Delta t}\left\|\mathbf{v}^{\mathrm{T}}(t)\right\|\mathrm{d}t}{D_{\mathrm{c}}^{\mathrm{t}}}\right]\right\}^2-1}{1024\left\{1-\exp\left[\frac{-\lambda_{\mathrm{R}}\int_t^{t+\Delta t}\left\|\mathbf{v}^{\mathrm{T}}(t)\right\|\mathrm{d}t}{D_{\mathrm{c}}^{\mathrm{t}}}\right]\right\}^4}} \tag{37}$$

$$r_{\mathrm{t},d/j}^{\mathrm{DS/DM,T}}(t)=\left\{\sqrt[3]{\xi_{\mathrm{time},d/j}^{\mathrm{DS/DM,T}}(t)+\sigma_{\mathrm{time},d/j}^{\mathrm{DS/DM,T}}(t)}+\sqrt[3]{\xi_{\mathrm{time},d/j}^{\mathrm{DS/DM,T}}(t)-\sigma_{\mathrm{time},d/j}^{\mathrm{DS/DM,T}}(t)}+\frac{1}{4\left\{1-\exp\left[\frac{-\lambda_{\mathrm{R}}\int_t^{t+\Delta t}\left\|\mathbf{v}_{d/j}^{\mathrm{DS/DM,T}}(t)-\mathbf{v}^{\mathrm{T}}(t)\right\|\mathrm{d}t}{D_{\mathrm{c}}^{\mathrm{t}}}\right]\right\}}\right\} \tag{43}$$
$$\times\int_t^{t+\Delta t}\left\|\mathbf{v}_{d/j}^{\mathrm{DS/DM,T}}(t)-\mathbf{v}^{\mathrm{T}}(t)\right\|\mathrm{d}t$$

with

$$\xi_{\mathrm{time},d/j}^{\mathrm{DS/DM,T}}(t)=\frac{-2\left\{1-\exp\left[\frac{-\lambda_{\mathrm{R}}\int_t^{t+\Delta t}\left\|\mathbf{v}_{d/j}^{\mathrm{DS/DM,T}}(t)-\mathbf{v}^{\mathrm{T}}(t)\right\|\mathrm{d}t}{D_{\mathrm{c}}^{\mathrm{t}}}\right]\right\}^2+1}{64\left\{1-\exp\left[\frac{-\lambda_{\mathrm{R}}\int_t^{t+\Delta t}\left\|\mathbf{v}_{d/j}^{\mathrm{DS/DM,T}}(t)-\mathbf{v}^{\mathrm{T}}(t)\right\|\mathrm{d}t}{D_{\mathrm{c}}^{\mathrm{t}}}\right]\right\}^3} \tag{44}$$

$$\sigma_{\mathrm{time},d/j}^{\mathrm{DS/DM,T}}(t)=\sqrt{\frac{\left\{1-\exp\left[\frac{-\lambda_{\mathrm{R}}\int_t^{t+\Delta t}\left\|\mathbf{v}_{d/j}^{\mathrm{DS/DM,T}}(t)-\mathbf{v}^{\mathrm{T}}(t)\right\|\mathrm{d}t}{D_{\mathrm{c}}^{\mathrm{t}}}\right]\right\}^2-1}{1024\left\{1-\exp\left[\frac{-\lambda_{\mathrm{R}}\int_t^{t+\Delta t}\left\|\mathbf{v}_{d/j}^{\mathrm{DS/DM,T}}(t)-\mathbf{v}^{\mathrm{T}}(t)\right\|\mathrm{d}t}{D_{\mathrm{c}}^{\mathrm{t}}}\right]\right\}^4}}. \tag{45}$$

that all dynamic clusters are observable at initial time t_0 and shrinkage factors are given by

$$\varepsilon_{\mathrm{time}}^{\mathrm{DS,T}}=\max\left\{\frac{D_{Od}^{\mathrm{DS,T}}(t_0)}{r_{\mathrm{t}}^{\mathrm{DS,T}}(t_0)}\right\},d=1,2,3,\cdots,D\left(t_0\right) \tag{46}$$

$$\varepsilon_{\mathrm{time}}^{\mathrm{DM,T}}=\max\left\{\frac{D_{Oj}^{\mathrm{DM,T}}(t_0)}{r_{\mathrm{t}}^{\mathrm{DM,T}}(t_0)}\right\},j=1,2,3,\cdots,J\left(t_0\right). \tag{47}$$

Condition of the time observable dynamic single/twin-cluster is similar to that of time observable static single/twin-cluster.

Therefore, the developed method considers the effects of VTD and continuously arbitrary trajectories. First, the developed method considers the difference in observable conditions caused by the difference in velocities between dynamic and static clusters. Second, continuous arbitrary trajectories of transceivers and dynamic clusters are characterized when computing time survival probabilities and radii of observable spheres assigned to static and dynamic clusters.

C. Soft Transition Factor

The power of clusters is given as [10]

$$P_n^{\mathrm{type}}(t)=\exp\left[-\tau_n^{\mathrm{type}}(t)\frac{r_\tau-1}{r_\tau\mathrm{DS}}\right]10^{-\frac{Z_n}{10}} \tag{48}$$

where type means the type of clusters, i.e., SS/DS/SM/DM, n is the n-th cluster, i.e., $s/d/i/j$, r_τ is the delay scaling parameter, DS is a random delay spread, and Z_n obeys the Gaussian distribution $\mathcal{N}(0,3)$. In the channel model [20], for each cluster, when it is switched from the observable state to the unobservable state, its power abruptly changes to 0, resulting in hard cluster power handover. On the contrary, when the cluster changes between observable and unobservable, its power changes continuously, i.e., soft cluster power handover. Meanwhile, when the center of transceiver antenna array is closer to the center of observable sphere, the power of the cluster assigned to this observable sphere is higher [21]. To mimic this phenomenon, a soft transition factor is introduced

$$\begin{aligned}P_n^{\mathrm{type,T/R}}(t)&=\Omega_n^{\mathrm{type,T/R}}(t)P_n^{\mathrm{type}}(t)\\&=\sin^2\left\{\frac{\pi}{2}\left[1-\frac{\bar{D}_{On}^{\mathrm{type,T/R}}(t)}{r_{\mathrm{t}}^{\mathrm{type,T/R}}(t)}\right]\right\}\exp\left[-\tau_n^{\mathrm{type}}(t)\frac{r_\tau-1}{r_\tau\mathrm{DS}}\right]10^{-\frac{Z_n}{10}}\end{aligned} \tag{49}$$

Since the soft transition factor obeys the squared sine function, which is a uniform continuity function, it can capture soft cluster power handover [15]. Only when the cluster is both an array observable cluster and a time observable cluster can it be an effective cluster, which contributes to the CIR. Note that the power of ineffective clusters is 0.

D. Frequency-Dependent Factor

In mmWave channels, the uncorrelated scattering assumption, which is used in sub-6 GHz, no longer holds, leading to frequency non-stationarity. To characterize channels in the frequency domain, time-varying transfer function (TVTF) is derived by adopting the Fourier transform to the CIR $h_{qp}(t,\tau)$. To mimic frequency non-stationarity, the frequency-dependent path gain should be captured [30]. A frequency-dependent factor is employed in the TVTF to model frequency non-stationarity, which is given as (50), shown at the top of the next page, where ε denotes a frequency-dependent factor associated with vehicular scenarios [31]. Based on the measurement and analysis in [20], [32] the interaction between clusters and multipaths with different wavelengths results in the frequency-dependence of rays. As a consequence, the frequency-dependence part $\left(\frac{f}{f_c}\right)^{\varepsilon}$ has an impact on the NLoS component, which is generated by clusters and multipaths with different wavelengths.

Similar to [18], the newly generated static/dynamic single/twin-clusters are taken into account. In summary, by using the visibility region-based method and constructing observable semi-spheres and observable spheres, the smooth cluster evolution in the space and time domains is modeled, thus mimicking space-time non-stationarity with T-S consistency. Due to the descent generality of the birth-death process method, it is embedded in the visibility region-based method. Soft transition factor and frequency-dependent factor are developed to model soft cluster power handover and frequency non-stationarity, respectively.

IV. Statistical Properties

Channel statistics, i.e., the S-T-F correlation function (STF-CF), power delay profile, time stationary interval, and Doppler power spectral density (DPSD), are derived.

A. Space-Time-Frequency Correlation Function

With the help of the derived TVTF in (50), the STF-CF is computed by [33]

$$\rho_{qp,q'p'}(t,f;\Delta t,\Delta f,\delta_{\mathrm{T}},\delta_{\mathrm{R}}) = \mathbb{E}[H^{*}_{qp}(t,f)H_{q'p'}(t+\Delta t,f+\Delta f)] \tag{51}$$

where $\mathbb{E}[\cdot]$ represents the expectation operation and $(\cdot)^{*}$ represents the complex conjugate operation. The LoS, GR, as well as static/dynamic single/multi-bouncing components are regarded as independent of each other [20], [34]. Hence, the STF-CF can be expressed by (52)–(58), shown at the top of the next page. Certainly, the derived STF-CF is S-T-F-varying, which demonstrated S-T-F non-stationarity of the proposed IS-GBSM. The STF-CF is simplified to the spatial cross-correlation function (SCCF) at Tx/Rx through setting $\Delta t = 0$, $\Delta f = 0$, as well as $p \neq p'/p = p'$, $q = q'/q \neq q'$. The STF-CF can be simplified to the temporal auto-correlation function (TACF) through setting $\Delta f = 0$, $p = p'$, as well as $q = q'$. The STF-CF is simplified to the frequency correlation function (FCF) through setting $\Delta t = 0$, $p = p'$, as well as $q = q'$.

B. Power Delay Profile

Power delay profile shows the power and delay of multipath components and is given by

$$\begin{aligned}\Theta(t,\tau) =& \sum_{s=1}^{S(t)}\sum_{n_s=1}^{N_s(t)} P^{\mathrm{SS}}_{s,n_s}(t)\delta\left(\tau-\tau^{\mathrm{SS}}_{s,n_s}(t)\right)\\ &+\sum_{d=1}^{D(t)}\sum_{n_d=1}^{N_d(t)} P^{\mathrm{DS}}_{d,n_d}(t)\delta\left(\tau-\tau^{\mathrm{DS}}_{d,n_d}(t)\right)\\ &+\sum_{i=1}^{I(t)}\sum_{n_i=1}^{N_i(t)} P^{\mathrm{SM}}_{i,n_i}(t)\delta\left(\tau-\tau^{\mathrm{SM}}_{i,n_i}(t)\right)\\ &+\sum_{j=1}^{J(t)}\sum_{n_j=1}^{N_j(t)} P^{\mathrm{DM}}_{j,n_j}(t)\delta\left(\tau-\tau^{\mathrm{DM}}_{j,n_j}(t)\right).\end{aligned} \tag{59}$$

Obviously, the derived power delay profile of the proposed IS-GBSM is time-varying.

C. Time Stationary Interval

The channel amplitude response is regarded as time stationary within the time stationary interval, which is the maximum period when the auto-correlation function of the power delay profile exceeds a threshold $\epsilon_{\mathrm{threshold}}$, e.g., 80% [35]. The time stationary interval is expressed by

$$\varrho(t) = \inf\{\Delta t|_{\Upsilon(t,\Delta t)\leq\epsilon_{\mathrm{threshold}}}\} \tag{60}$$

where $\Upsilon(t,\Delta t)$ represents the auto-correlation function of the power delay profile

$$\Upsilon^{\mathrm{T}}(t,\Delta t) = \frac{\int\Theta(t,\tau)\Theta(t+\Delta t,\tau)\mathrm{d}\tau}{\max\{\int\Theta^2(t,\tau)\mathrm{d}\tau,\int\Theta^2(t+\Delta t,\tau)\mathrm{d}\tau\}}. \tag{61}$$

D. Doppler Power Spectral Density

The DPSD is obtained through taking Fourier transfer of TACF and is expressed by

$$\Omega_{qp}(t;f_d) = \int_{-\infty}^{+\infty}\rho_{qp}(t;\Delta t)e^{-j2\pi f_d\Delta t}\mathrm{d}(\Delta t) \tag{62}$$

where $\rho_{qp}(t;\Delta t)$ is the TACF and f_d is the Doppler shift.

V. Results and Analysis

In this section, typical channel statistical properties are simulated and compared with the measurement/RT-based results. Key channel-related parameters are given below. The uniform linear antenna array is utilized in the simulation and the adjacent antenna spacing is $\delta_{\mathrm{T}} = \delta_{\mathrm{R}} = 0.5\ \lambda$. The frequency-dependent factor is $\varepsilon = 1.45$ [31]. Abstracted delays $\tilde{\tau}^{\mathrm{SM}}_{qp,i,n_i}(t)$ and $\tilde{\tau}^{\mathrm{DM}}_{qp,j,n_j}(t)$ obey the exponential distribution with the mean and variance 80 ns and 15 ns [36]. The number of rays in clusters obeys Poisson distribution with mean and variance $\tilde{\lambda} = 15$ [37]. The heights of transceiver antenna are $\xi_{\mathrm{T}} = \xi_{\mathrm{R}} = 2$ m. Other key channel-related parameters are listed in Table I.

$$
\begin{aligned}
H_{qp}(t,f) = &\sqrt{\frac{K(t)}{K(t)+1}} h_{qp}^{\mathrm{LoS}}(t) \exp\left[-j2\pi f \tau_{qp}^{\mathrm{LoS}}(t)\right] + \sqrt{\frac{\eta^{\mathrm{GR}}(t)}{K(t)+1}} \left(\frac{f}{f_c}\right)^{\varepsilon} h_{qp}^{\mathrm{GR}}(t) \exp\left[-j2\pi f \tau_{qp}^{\mathrm{GR}}(t)\right] \\
&+ \sqrt{\frac{\eta^{\mathrm{SS}}(t)}{K(t)+1}} \left(\frac{f}{f_c}\right)^{\varepsilon} \sum_{s=1}^{S(t)} \sum_{n_s=1}^{N_s(t)} h_{qp,s,n_s}^{\mathrm{SS}}(t) \exp\left[-j2\pi f \tau_{qp,s,n_s}^{\mathrm{SS}}(t)\right] + \sqrt{\frac{\eta^{\mathrm{SM}}(t)}{K(t)+1}} \left(\frac{f}{f_c}\right)^{\varepsilon} \sum_{i=1}^{I(t)} \sum_{n_i=1}^{N_i(t)} h_{qp,i,n_i}^{\mathrm{SM}}(t) \exp\left[-j2\pi f \tau_{qp,i,n_i}^{\mathrm{SM}}(t)\right] \\
&+ \sqrt{\frac{\eta^{\mathrm{DS}}(t)}{K(t)+1}} \left(\frac{f}{f_c}\right)^{\varepsilon} \sum_{d=1}^{D(t)} \sum_{n_d=1}^{N_d(t)} h_{qp,d,n_d}^{\mathrm{DS}}(t) \exp\left[-j2\pi f \tau_{qp,d,n_d}^{\mathrm{DS}}(t)\right] + \sqrt{\frac{\eta^{\mathrm{DM}}(t)}{K(t)+1}} \left(\frac{f}{f_c}\right)^{\varepsilon} \sum_{j=1}^{J(t)} \sum_{n_j=1}^{N_j(t)} h_{qp,j,n_j}^{\mathrm{DM}}(t) \exp\left[-j2\pi f \tau_{qp,j,n_j}^{\mathrm{DM}}(t)\right]
\end{aligned} \tag{50}
$$

$$
\begin{aligned}
\rho_{qp,q'p'}(t,f;\Delta t,\Delta f,\delta_{\mathrm{T}},\delta_{\mathrm{R}}) = &\rho_{qp,q'p'}^{\mathrm{LoS}}(t,f;\Delta t,\Delta f,\delta_{\mathrm{T}},\delta_{\mathrm{R}}) + \rho_{qp,q'p'}^{\mathrm{GR}}(t,f;\Delta t,\Delta f,\delta_{\mathrm{T}},\delta_{\mathrm{R}}) + \rho_{qp,q'p'}^{\mathrm{SS}}(t,f;\Delta t,\Delta f,\delta_{\mathrm{T}},\delta_{\mathrm{R}}) \\
&+ \rho_{qp,q'p'}^{\mathrm{DS}}(t,f;\Delta t,\Delta f,\delta_{\mathrm{T}},\delta_{\mathrm{R}}) + \rho_{qp,q'p'}^{\mathrm{SM}}(t,f;\Delta t,\Delta f,\delta_{\mathrm{T}},\delta_{\mathrm{R}}) + \rho_{qp,q'p'}^{\mathrm{DM}}(t,f;\Delta t,\Delta f,\delta_{\mathrm{T}},\delta_{\mathrm{R}})
\end{aligned} \tag{52}
$$

with

$$
\rho_{qp,q'p'}^{\mathrm{LoS}}(t,f;\Delta t,\Delta f,\delta_{\mathrm{T}},\delta_{\mathrm{R}}) = \sqrt{\frac{K(t)K(t+\Delta t)}{(K(t)+1)(K(t+\Delta t)+1)}} h_{qp}^{\mathrm{LoS}*}(t) h_{q'p'}^{\mathrm{LoS}}(t+\Delta t) e^{j2\pi[f\tau_{qp}^{\mathrm{LoS}}(t) - (f+\Delta f)\tau_{qp}^{\mathrm{LoS}}(t+\Delta t)]} \tag{53}
$$

$$
\rho_{qp,q'p'}^{\mathrm{GR}}(t,f;\Delta t,\Delta f,\delta_{\mathrm{T}},\delta_{\mathrm{R}}) = \sqrt{\frac{\eta^{\mathrm{GR}}(t)\eta^{\mathrm{GR}}(t+\Delta t)}{(K(t)+1)(K(t+\Delta t)+1)}} h_{qp}^{\mathrm{GR}*}(t) h_{q'p'}^{\mathrm{GR}}(t+\Delta t) e^{j2\pi[f\tau_{qp}^{\mathrm{GR}}(t) - (f+\Delta f)\tau_{qp}^{\mathrm{GR}}(t+\Delta t)]} \tag{54}
$$

$$
\begin{aligned}
&\rho_{qp,q'p'}^{\mathrm{SS}}(t,f;\Delta t,\Delta f,\delta_{\mathrm{T}},\delta_{\mathrm{R}}) = \\
&\sqrt{\frac{\eta^{\mathrm{SS}}(t)\eta^{\mathrm{SS}}(t+\Delta t)}{(K(t)+1)(K(t+\Delta t)+1)}} \mathbb{E}\left[\sum_{s=1}^{S(t)} \sum_{s'=1}^{S(t+\Delta t)} \sum_{n_s=1}^{N_s(t)} \sum_{n_s'=1}^{N_s(t+\Delta t)} h_{qp,s,n_s}^{\mathrm{SS}*}(t) h_{q'p',s',n_s'}^{\mathrm{SS}}(t+\Delta t) e^{j2\pi[f\tau_{qp,s,n_s}^{\mathrm{SS}}(t) - (f+\Delta f)\tau_{q'p',s',n_s'}^{\mathrm{SS}}(t+\Delta t)]}\right]
\end{aligned} \tag{55}
$$

$$
\begin{aligned}
&\rho_{qp,q'p'}^{\mathrm{DS}}(t,f;\Delta t,\Delta f,\delta_{\mathrm{T}},\delta_{\mathrm{R}}) = \\
&\sqrt{\frac{\eta^{\mathrm{DS}}(t)\eta^{\mathrm{DS}}(t+\Delta t)}{(K(t)+1)(K(t+\Delta t)+1)}} \mathbb{E}\left[\sum_{d=1}^{D(t)} \sum_{d'=1}^{D(t+\Delta t)} \sum_{n_d=1}^{N_d(t)} \sum_{n_d'=1}^{N_d(t+\Delta t)} h_{qp,d,n_d}^{\mathrm{DS}*}(t) h_{q'p',d',n_d'}^{\mathrm{DS}}(t+\Delta t) e^{j2\pi[f\tau_{qp,d,n_d}^{\mathrm{DS}}(t) - (f+\Delta f)\tau_{q'p',d',n_d'}^{\mathrm{DS}}(t+\Delta t)]}\right]
\end{aligned} \tag{56}
$$

$$
\begin{aligned}
&\rho_{qp,q'p'}^{\mathrm{SM}}(t,f;\Delta t,\Delta f,\delta_{\mathrm{T}},\delta_{\mathrm{R}}) = \\
&\sqrt{\frac{\eta^{\mathrm{SM}}(t)\eta^{\mathrm{SM}}(t+\Delta t)}{(K(t)+1)(K(t+\Delta t)+1)}} \mathbb{E}\left[\sum_{i=1}^{I(t)} \sum_{i'=1}^{I(t+\Delta t)} \sum_{n_i=1}^{N_i(t)} \sum_{n_i'=1}^{N_i(t+\Delta t)} h_{qp,i,n_i}^{\mathrm{SM}*}(t) h_{q'p',i',n_i'}^{\mathrm{SM}}(t+\Delta t) e^{j2\pi[f\tau_{qp,i,n_i}^{\mathrm{SM}}(t) - (f+\Delta f)\tau_{q'p',i',n_i'}^{\mathrm{SM}}(t+\Delta t)]}\right]
\end{aligned} \tag{57}
$$

$$
\begin{aligned}
&\rho_{qp,q'p'}^{\mathrm{DM}}(t,f;\Delta t,\Delta f,\delta_{\mathrm{T}},\delta_{\mathrm{R}}) = \\
&\sqrt{\frac{\eta^{\mathrm{DM}}(t)\eta^{\mathrm{DM}}(t+\Delta t)}{(K(t)+1)(K(t+\Delta t)+1)}} \mathbb{E}\left[\sum_{j=1}^{J(t)} \sum_{j'=1}^{J(t+\Delta t)} \sum_{n_j=1}^{N_j(t)} \sum_{n_j'=1}^{N_j(t+\Delta t)} h_{qp,j,n_j}^{\mathrm{DM}*}(t) h_{q'p',j',n_j'}^{\mathrm{DM}}(t+\Delta t) e^{j2\pi[f\tau_{qp,j,n_j}^{\mathrm{DM}}(t) - (f+\Delta f)\tau_{q'p',j',n_j'}^{\mathrm{DM}}(t+\Delta t)]}\right].
\end{aligned} \tag{58}
$$

TABLE I
KEY CHANNEL-RELATED PARAMETERS IN THE SIMULATION.

Symbol	Fig. 3	Fig. 4	Fig. 5	Fig. 6	Fig. 7	Fig. 8	Fig. 10	Fig. 11	Fig. 13
f_c (GHz)	28	28	28	38	38	28	1.8	1.8	28
BW (GHz)	2	2	2	4	4	2	0.015	0.015	2
$M_{\mathrm{T}}, M_{\mathrm{R}}$	32, 32	32, 32	32, 32	32, 40	40, 32	32, 40	1, 16	1, 16	32, 32
K	0.04	0.03	0.05	0.1	0.09	0.1	0.1	0.1	0.06
$D_{\mathrm{cen}}(0)$ (m)	100	120	70	130	150	125	500	500	85
$v^{\mathrm{T}}(0), v^{\mathrm{R}}(0)$ (m/s)	15, 20	14, 15	22, 17	25, 24	10, 12	11, 9	0, 16	0, 16	12, 10
$\bar{v}_d^{\mathrm{DS}}(0)$ (m/s)	2	3	2	5	3.5	4	2	2	4
$\bar{v}_j^{\mathrm{DM,T}}(0), \bar{v}_j^{\mathrm{DM,R}}(0)$ (m/s)	6, 7	8, 8	9, 11	16, 16	12, 12	12, 13	8, 8	8, 8	12, 12
$\epsilon_{\mathrm{SDI}}(0)$	(a): 1/2 (b): 2	(a): 6/11 (b): 11/6	(a): 3/5 (b): 5/3	(a): 7/12 (b): 12/7	(a): 4/5 (b): 5/4	1	8/7	8/7	(a): 6/11 (b): 11/6
$\epsilon_{\mathrm{VDI}}(0)$	4/5	(a): 7/10 (b): 10/7	7/9	7/12	(a): 7/11 (b): 11/7	1	(a): 2/3 (b): 3/2	(a): 2/3 (b): 3/2	7/10
t (s)	0	1	2	1.5	0	(a): 0.03 (b): 0	0	0	0
$A_p^{\mathrm{T}}, A_q^{\mathrm{R}}$	$A_2^{\mathrm{T}}, A_{31}^{\mathrm{R}}$	$A_{20}^{\mathrm{T}}, A_1^{\mathrm{R}}$	$A_1^{\mathrm{T}}, A_1^{\mathrm{R}}$	(a): $A_1^{\mathrm{T}}, A_8^{\mathrm{R}}$ (b): $A_1^{\mathrm{T}}, A_{13}^{\mathrm{R}}$	$A_1^{\mathrm{T}}, A_1^{\mathrm{R}}$	(a): -, A_7^{R} (b): -,-	A_1^{T}, –	$A_1^{\mathrm{T}}, A_2^{\mathrm{R}}$	$A_1^{\mathrm{T}}, A_1^{\mathrm{R}}$

A. Simulation of Channel Statistical Properties

In Fig. 3, the TACF under sparse/rich SE with the acceleration/deceleration VMT of transceivers is illustrated. In the rich SE, it is obvious that the number of twin-clusters is larger than that of single-clusters. In this case, compared to the sparse SE, the number of propagation paths is also larger in the rich SE. As a result, the rich SE is more complex and the corresponding TACF is lower than that under the sparse SE. TACF with deceleration VMTs is higher than that with acceleration VMTs. The underlying reason is that the deceleration VMTs of transceivers leads to more stable V2V communication environment.

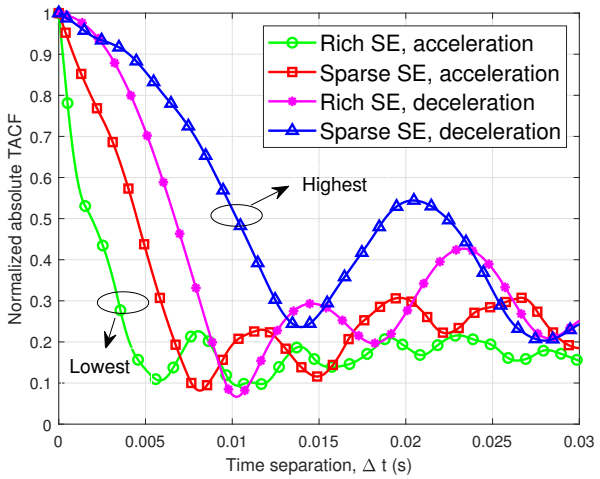

Fig. 3. TACF under sparse/rich SE with the acceleration/deceleration VMT.

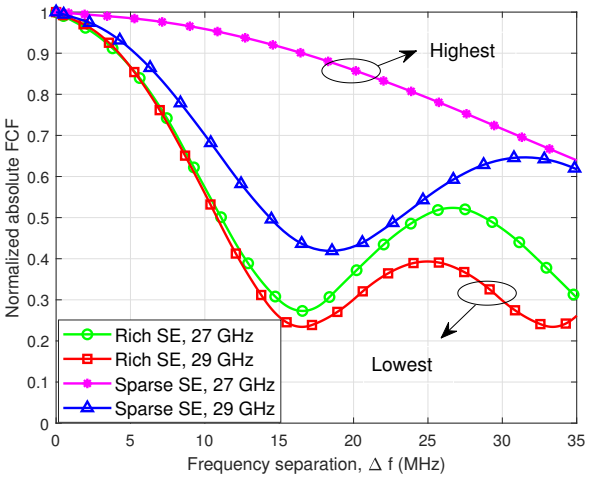

Fig. 5. FCF under sparse/rich SE at different frequencies.

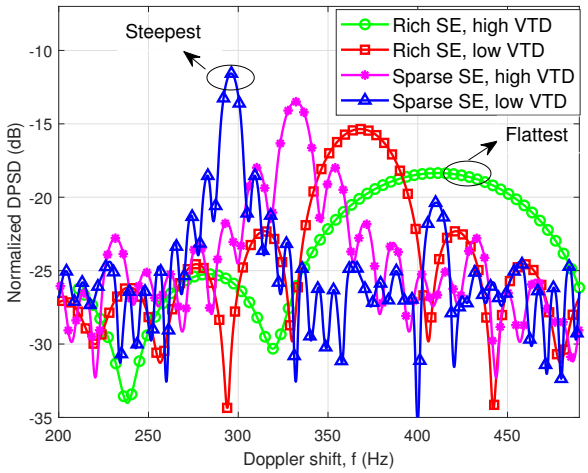

Fig. 4. DPSD under sparse/rich SE with high/low VTD.

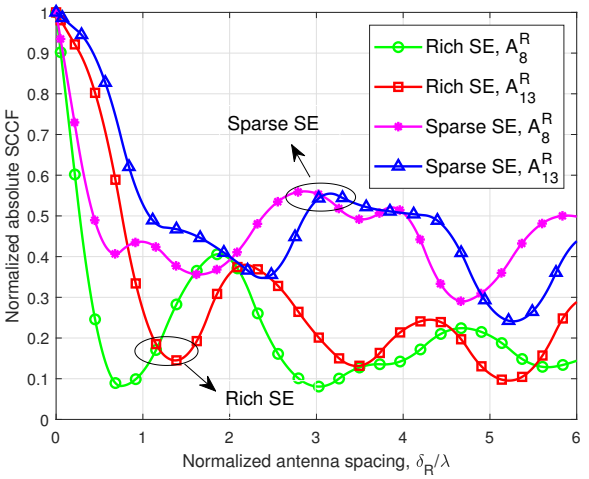

Fig. 6. SCCF under sparse/rich SE at different frequencies.

The DPSD under sparse/rich SE with high/low VTD is given in Fig. 4. Among these DPSDs, the DPSD under rich SE with high VTD exhibits the flattest distribution, while the DPSD under sparse SE with low VTD exhibits the steepest distribution. The philosophy is that the received power in V2V communications under rich SE with high VTD tends to come from clusters in all directions. Nonetheless, in the sparse SE with low VTD, the received power concentrates on several Doppler frequencies.

Fig. 5 presents the FCF under sparse/rich SE at different frequencies. Owing to the modeling of the frequency-dependent path gain, the FCF is frequency-variant, where the FCF at $f = 29$ GHz is lower than that at $f = 27$ GHz. The FCF is a function of frequency separation Δf and frequency f, thus mimicking frequency non-stationarity and frequency selectivity. In contrast, the FCF under rich SE is lower than that under sparse SE. This is because that, in rich SE, the multi-bouncing propagation is more dominant and the delay spread is severer, resulting in more obvious channel frequency selectivity and lower FCF.

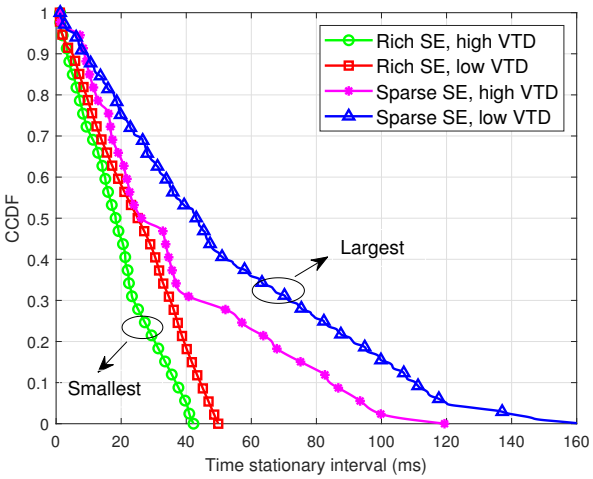

Fig. 7. CCDF of TSI under sparse/rich SE with high/low VTD.

In Fig. 6, the Rx SCCF under sparse/rich at different

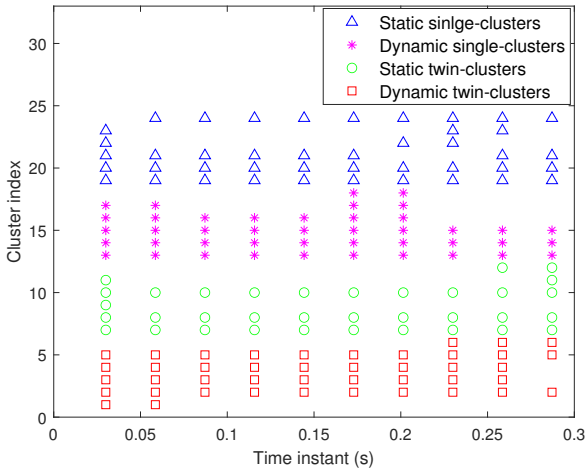

(a)

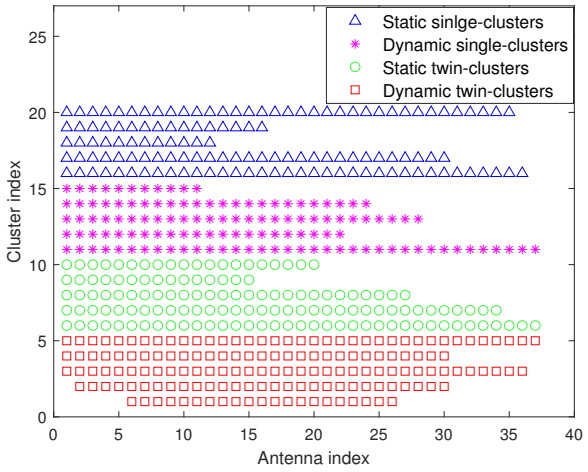

(b)

Fig. 8. Cluster evolution at Rx. (a) Time axis. (b) Array axis.

reference antennas is depicted. The numbers of Tx and Rx antennas are 32 and 40, respectively, which can be regarded as a massive MIMO scenario [29]. The SCCF depends on both the antenna spacing and reference antennas, and hence space non-stationarity brought by massive MIMO is imitated. In addition, compared to the rich SE, the SCCF under the sparse SE is higher. The physical reason is that more single-clusters lead to smaller number of propagation paths, smaller channel spatial diversity, and higher SCCF.

Fig. 7 gives the complementary cumulative distribution function (CCDF) of time stationary interval under sparse/rich SE with high/low VTD. Since there are more highly mobile vehicles in high VTD, the V2V communication scenario is more rapidly-changing, resulting in lower time stationary interval. Furthermore, attributed to more complex propagation in rich SE, the time stationary interval under rich SE is lower than that under sparse SE. Therefore, the V2V channel under rich SE with high VTD exhibits the smallest time stationary interval, whereas the largest time stationary interval under sparse SE with low VTD.

(a) (b)

Fig. 9. Vehicular channel measurement campaign. (a) Measurement van with a real antenna array. (b) Measurement scenario.

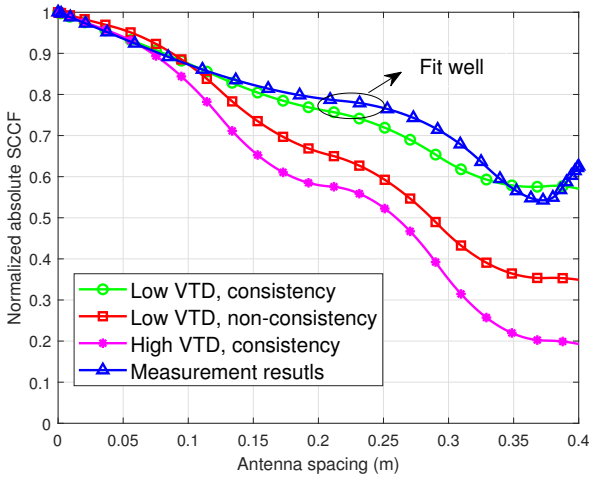

Fig. 10. Comparison of the simulated SCCF and the measured SCCF in [38].

Cluster time and array evolution are shown in Figs. 8 (a) and (b), respectively. The numbers of static/dynamic single/twin-clusters are $S(0) = D(0) = I(0) = J(0) = 5$ at initial time. In Fig. 8(a), the simulation time is from 0.03 s to 0.28 s and the selected antenna is A_7^{R}, where newly generated clusters can be observed. In Fig. 8(b), the simulation time is the initial time, i.e., $t = 0$ s. By exploiting the developed method, cluster evolution is smooth and consistent as time and array evolve. In this case, adjacent time instants and antenna elements have similar observable cluster sets, and hence channel T-S consistency is embedded in the proposed IS-GBSM.

B. Model Validation by Measurement and RT-Based Results

To validate the generality of the proposed model, we conducted a vehicular channel measurement in a vicinity of Aalborg, Denmark with the carrier frequency $f_c = 1.8$ GHz and bandwidth 15 MHz [38]. It is clear that 1.8 GHz is a typical frequency band of Long Term Evolution (LTE) vehicle-to-everything (V2X) and is utilized for the carrier frequency of vehicular channel measurement. As shown in Fig. 9(a), a real antenna array with sixteen antennas was equipped on the roof of a van, which can be regarded as a multi-antenna vehicular measurement. In the measurement, many routes were considered, and the *dominant rural in Route 1*, i.e., green dots in Fig. 9(b), was chosen for comparison with the simulation results.

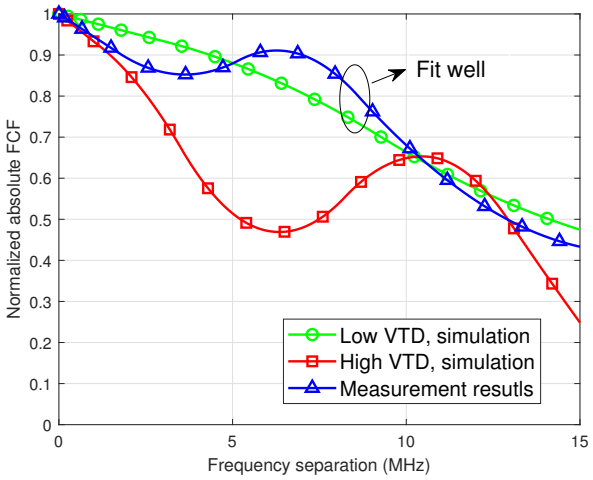

Fig. 11. Comparison of the simulated FCF and the measured FCF in [38].

The measured CIR is processed to obtain the measured SCCF, which is compared with the simulated SCCF in Fig. 10.[1] Furthermore, since the measurement scenario was a dominant rural, it can be regarded as a low VTD scenario. The simulated SCCF with channel consistency at low VTD fits well with measurement. Nonetheless, as the spatial correlation is underestimated by randomly characterizing the cluster array evolution, the simulated SCCF without channel consistency is lower than the measurement. Also, the simulated SCCF with high VTD is lower than the measurement. This is because that more vehicles, i.e., more dynamic clusters, around the transceiver lead to more propagation paths, larger channel spatial diversity, and smaller SCCF. As a result, by considering the effect of VTDs and capturing channel consistency, the proposed model can accurately reflect the reality.

To validate the existence of frequency selectivity in the channel measurement scenario [38] with the carrier frequency $f_c = 1.8$ GHz and bandwidth 15 MHz, the measured CIR is processed to obtain the measured FCF. From Fig. 11, it can be observed that the measured FCF depends on the frequency separation Δf, and exhibits fluctuations in the frequency domain, which validates the existence of frequency selectivity in the channel measurement scenario. This is because that the multipath effect is obvious in complex vehicular communication scenarios, where the channel coherence bandwidth is small. In this case, the channel can exhibit frequency selectivity within the measurement bandwidth. Furthermore, the measured and simulated FCFs are compared. The close agreement between the measured FCF and the simulated FCF at low VTD is achieved. However, the FCF at high VTD is lower than that at low VTD as the V2V channel is more complex at high VTD.

[1]Although the proposed IS-GBSM is based on the uniform linear antenna and the vehicular channel measurement utilizes the uniform circular array, the antenna array used in the simulation does not affect the output curve. This is because that power angular spectrum is a propagation channel characteristic, which is physically determined by the stochastic properties of the clusters exist in the scenario. Meanwhile, SCCF and power angular spectrum are Fourier transform pairs. Consequently, the comparison of simulated SCCF and measured SCCF is proper.

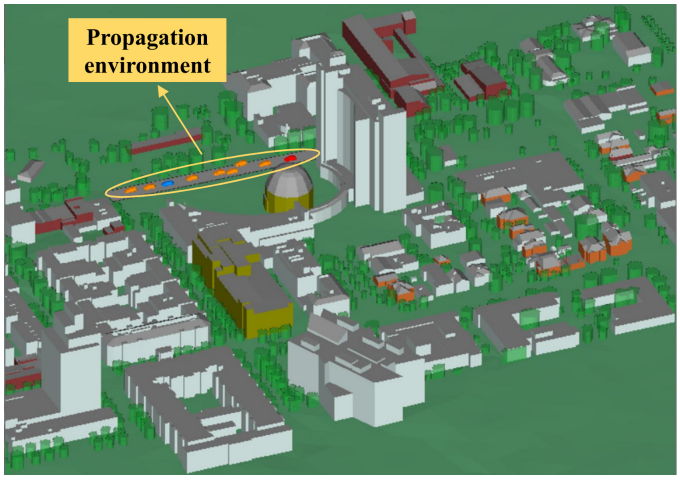

(a)

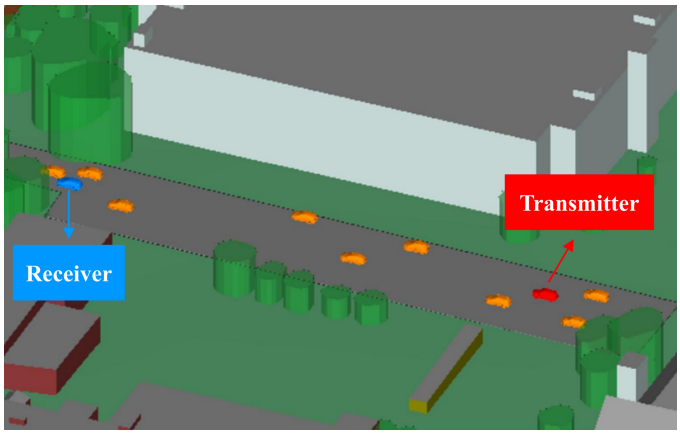

(b)

Fig. 12. V2V communication scenario in Wireless Insite. (a) Scenario in San Jose, California, the United States. (b) Transceiver propagation environment.

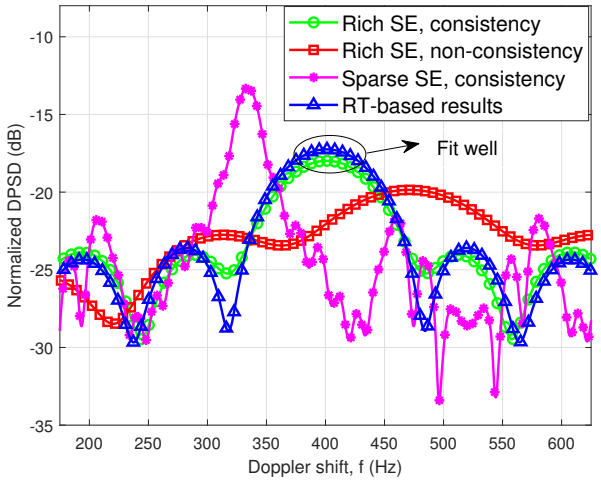

Fig. 13. Comparison of the simulated DPSD and RT-based DPSD.

To further verify the accuracy of the developed IS-GBSM, the RT-based method is used. Since the RT-based method generates channel parameters according to the geometrical

optics and uniform theory of diffraction, the RT-based result is of high fidelity and is widely utilized to validate the accuracy of the proposed channel models [40], [41]. Specifically, a *massive MIMO mmWave* V2V communication scenario is constructed by the RT tool, i.e., Wireless InSite [39]. In Fig. 12(a), the scenario is given, which is in San Jose, California, the United States. In Fig. 12(b), the propagation environment is depicted, where there are dynamic vehicles and static trees and buildings. In the Wireless InSite simulation platform, the carrier frequency is set to $f_c = 28$ GHz with 2 GHz bandwidth for mimicking the high frequency and wide band in mmWave communications. The numbers of antenna elements are $M_{\mathrm{T}} = M_{\mathrm{R}} = 32$. The spacing of adjacent antennas is half wavelength.

The simulated and RT-based DPSDs are compared in Fig. 13. The propagation environment can be regarded as a rich SE with high VTD according to Fig. 12(b). The simulated DPSD under rich SE with channel consistency fits well with the RT-based DPSD. Nonetheless, when the birth-death process method used in [8], [17], [20] is exploited, the evolution of clusters is random rather than smooth, resulting in channel non-consistency. Under this condition, the DPSD distribution is flatter, attributed to more random and dispersed distribution of clusters in the environment. Also, compared to rich SE, the simulated DPSD under sparse SE has a steeper distribution. Consequently, the necessities of capturing channel consistency and rich/sparse SE are demonstrated and the proposed model can accurately reflect the reality.

VI. Conclusions

This paper has proposed a novel 3D 6G channel model for mmWave massive MIMO V2V channels, where the mixed-bouncing propagation, GR, V2V scenarios with different VTDs, and continuously arbitrary VMTs have been considered. A new method has been developed, which can simultaneously imitate S-T-F non-stationarity of V2V channels with T-S consistency. Key channel statistics have been derived. Simulation results have shown that S-T-F non-stationarity and T-S consistency have been captured. Compared to low VTD, channels in high VTD have flatter distribution of DPSD, smaller time stationary interval, and lower SCCF. Meanwhile, compared to rich SE, channels in sparse SE have higher TACF, steeper distribution of DPSD, higher FCF, larger time stationary interval, and higher SCCF. The comparison between simulation results and measurement/RT-based results has verified the accuracy of the proposed model. The comparison has demonstrated that the capturing of channel consistency, high/low VTD, and rich/sparse SE is indispensable. In the future, with the development of measurement equipment, the massive MIMO mmWave V2V channel measurement campaign needs to be carried out to further validate the proposed IS-GBSM.

References

[1] X. Cheng, Z. Huang, and S. Chen, "Vehicular communication channel measurement, modelling, and application for beyond 5G and 6G," *IET Commun.*, vol. 14, no. 19, pp. 3303–3311, Nov. 2020.

[2] I. Sen and D. W. Matolak, "Vehicle-vehicle channel models for the 5-GHz band," *IEEE Trans. Intell. Transp. Syst.*, vol. 9, no. 2, pp. 235–245, Jun. 2008.

[3] R. He *et al.*, "Propagation channels of 5G millimeter-wave vehicle-to-vehicle communications: Recent advances and future challenges," *IEEE Veh. Technol. Mag.*, vol. 15, no. 1, pp. 16–26, Mar. 2020.

[4] H. Jiang, B. Xiong, H. Zhang, and E. Basar, "Hybrid far- and near-field modeling for reconfigurable intelligent surface assisted V2V channels: A sub-array partition based approach," *IEEE Trans. Wireless Commun.*, to be published. Doi: 10.1109/TWC.2023.3262063.

[5] L. Bai, Z. Huang, H. Du, and X. Cheng, "A 3-D non-stationary wideband V2V GBSM with UPAs for massive MIMO wireless communication systems," *IEEE Internet. Things. J.*, vol. 8, no. 24, pp. 17622–17638, Dec. 2021.

[6] X. Cheng, Z. Huang, and L. Bai, "Channel nonstationarity and consistency for beyond 5G and 6G: A survey," *IEEE Commun. Surveys Tutor.*, vol. 24, no. 3, pp. 1634–1669, third-quarter 2022.

[7] A. G. Zajic, G. L. Stüber, T. G. Pratt, and S. T. Nguyen, "Wideband MIMO mobile-to-mobile channels: Geometry-based statistical modeling with experimental verification," *IEEE Trans. Veh. Technol.*, vol. 58, no. 2, pp. 517–534, Jun. 2009.

[8] E. Michailidis, N. Nomikos, P. Trakadas, and A. G. Kanatas, "Three-dimensional modeling of mmWave doubly massive MIMO aerial fading channels," *IEEE Trans. Veh. Technol.*, vol. 69, no. 2, pp. 1190–1202, Feb. 2020.

[9] H. Jiang, B. Xiong, H. Zhang, and E. Basar, "Physics-based 3D end-to-end modeling for double-RIS assisted non-stationary UAV-to-ground communication channels," *IEEE Trans. Commun*, to be published. Doi: 10.1109/TCOMM.2023.3266832.

[10] *Technical Specification Group Radio Access Network; Study on Channel Model for Frequencies From 0.5 to 100 GHz (Release 14)*, document TR 38.901 Version 14.2.0, 3GPP, Sep. 2017. [Online]. Available: http://www.3gpp.org/DynaReport/38901.htm

[11] L. Bai, Z. Huang, and X. Cheng, "A 3D cluster-based channel model for 5G and beyond 5G vehicle-to-vehicle massive MIMO channels," *IEEE Trans. Vehicular Technol.*, vol. 70, no. 9, pp. 8401–8414, Sep. 2021.

[12] N. Ahmed, B. Hua, Q. Zhu, K. Mao, and J. Bao, "A novel GBSM for non-stationary V2V channels allowing 3D velocity variations," *Sensors*, vol. 21, no. 9, pp. 3271–3284, May 2021.

[13] B. Xiong *et al.*, "Novel multi-mobility V2X channel model in the presence of randomly moving clusters," *IEEE Trans. Wireless Commun.*, vol. 20, no. 5, pp. 3180–3195, May 2021.

[14] C. F. López and C.-X. Wang, "Novel 3-D non-stationary wideband models for massive MIMO channels," *IEEE Trans. Wireless Commun.*, vol. 17, no. 5, pp. 2893–2905, May 2021.

[15] S. Jaeckel, L. Raschkowski, K. Borner, and L. Thiele, "QuaDRiGa-Quasi Deterministic Radio Channel Generator, User Manual and Documentation," Fraunhofer Heinrich Hertz Institute, Tech. Rep. v2.4.0. 2020.

[16] A. F. Molisch, F. Tufvesson, J. Karedal, and C. F. Mecklenbrauker, "A survey on vehicle-to-vehicle propagation channels," *IEEE Wireless Commun.*, vol. 16, no. 6, pp. 12–22, Dec. 2009.

[17] Z. Huang and X. Cheng, "A 3D non-stationary model for beyond 5G and 6G vehicle-to-vehicle mmWave massive MIMO channels," *IEEE Trans. Intell. Transp. Syst.*, vol. 23, no. 7, pp. 8260–8276, Jul. 2022.

[18] Z. Huang, X. Cheng, and X. Yin, "A general 3D non-stationary 6G channel model with time-space consistency," *IEEE Trans. Commun.*, vol. 70, no. 5, pp. 3436–3450, May 2022.

[19] F. Ademaj, S. Schwarz, T. Berisha, and M. Rupp, "A spatial consistency model for geometry-based stochastic channels," *IEEE Access*, vol. 7, pp. 183414–183427, Dec. 2019.

[20] J. Bian, C.-X. Wang, X. Gao, X. You, and M. Zhang, "A general 3D non-stationary wireless channel model for 5G and beyond," *IEEE Trans. Wireless Commun.*, vol. 20, no. 5, pp. 3211–3224, May 2021.

[21] N. Cardona, *Cooperative Radio Communications for Green Smart Environments*. Gistrup, Denmark.: River Publishers, 2016.

[22] X. Cai, X. Cheng, and T. Fredrik, "Toward 6G with Terahertz communications: Understanding the propagation channels," *IEEE Commun. Mag.*, to be published, 2023.

[23] S. Gao, X. Cheng, and L. Yang, "Estimating doubly-selective channels for hybrid mmWave massive MIMO systems: A doubly-sparse approach," *IEEE Trans. Wireless Commun.*, vol. 19, no. 9, pp. 5703–5715, Sept. 2020.

[24] S. Jaeckel, L. Raschkowski, S. Wu, L. Thiele, and W. Keusgen, "An explicit ground reflection model for mm-Wave channels," in *Proc. IEEE WCNC'17*, San Francisco, CA, USA, Mar. 2017, pp. 1–5.

[25] R. Verdone and A. Zanella, *Pervasive Mobile and Ambient Wireless Communications*. London: Springer, 2012.

[26] M. Zhu, G. Eriksson, and F. Tufvesson, "The COST 2100 channel model: Parameterization and validation based on outdoor MIMO measurements at 300 MHz," *IEEE Trans. Wireless Commun.*, vol. 12, no. 2, pp. 888–897, Feb. 2013.
[27] J. Flordelis, X. Li, O. Edfors, and F. Tufvesson, "Massive MIMO extensions to the COST 2100 channel model: Modeling and validation," *IEEE Trans. Wireless Commun.*, vol. 19, no. 1, pp. 380–394, Jan. 2020.
[28] S. Wu, C.-X. Wang, H. Aggoune, M. M. Alwakeel, and Y. He, "A non-stationary 3-D wideband twin-cluster model for 5G massive MIMO channels," *IEEE J. Sel. Areas Commun.*, vol. 32, no. 6, pp. 1207–1446, Jun. 2014.
[29] S. Wu, C.-X. Wang, H. Aggoune, M. M. Alwakeel, and X.-H. You, "A general 3-D non-stationary 5G wireless channel model," *IEEE Trans. Commun.*, vol. 66, no. 7, pp. 3065–3078, Jul. 2018.
[30] D. He *et al.*, "Stochastic channel modeling for kiosk applications in the terahertz band," *IEEE Trans. Terahertz Sci. Technol.*, vol. 7, no. 5, pp. 502–513, Sep. 2017.
[31] A. F. Molisch, "A comprehensive model for ultrawideband propagation channels", in *Proc. IEEE GLOBECOM'05*, St. Louis, MO, USA, Dec. 2005, pp. 3648–3653.
[32] A. F. Molisch *et al.*, *IEEE 802.15.4a Channel Model-Final Report*, Tech. Rep., Document IEEE 802.1504-0062-02-004a, 2005.
[33] M. Patzold, *Mobile Radio Channels, 2nd ed.* West Sussex, U.K.: Wiley, 2012.
[34] Z. Huang *et al.*, "A LiDAR-aided vehicle-to-vehicle (V2V) channel model for sensing and communication integration," *IEEE Trans. Intell. Transp. Syst.*, 2023.
[35] C. Chen, Z. Zhong, and B. Ai, "Stationarity intervals of time-variant channel in high speed railway scenario," *J. China Commun.*, vol. 9, no. 8, pp. 64–70, Aug. 2012.
[36] L. Bai, Z. Huang, X. Zhang, and X. Cheng, "A 3D non-stationary model for 6G massive MIMO mmWave UAV channels," *IEEE Trans. Wireless Commun.*, vol. 21, no. 6, pp. 4325–4339, Jun. 2022.
[37] X. Wu *et al.*, "60-GHz millimeter-wave channel measurements and modeling for indoor office environments," *IEEE Trans. Antennas Propag.*, vol. 65, no. 4, pp. 1912–1924, Apr. 2017.
[38] T. Izydorczyk, F. M. L. Tavares, G. Berardinelli, M. Bucur, and P. Mogensen, "Performance evaluation of multi-antenna receivers for vehicular communications in live LTE networks," in *Proc. IEEE VTC'19*, Kuala Lumpur, Malaysia, Jun. 2019, pp. 1–6.
[39] *Remcom.* Wireless InSite. [Online]. Available: https://www.remcom.com/wireless-insite-em-propagation-software [Accessed date: Mar. 2022].
[40] K. Mao *et al.*, "Machine learning-based 3D channel modeling for U2V mmWave communications," *IEEE Internet Things J.*, vol. 9, no. 18, pp. 17592–17607, Sep. 2022.
[41] F. Ademaj, S. Schwarz, T. Berisha, and M. Rupp, "A spatial consistency model for geometry-based stochastic channels," *IEEE Access*, vol. 7, pp. 183414–183427, Dec. 2019.

Ziwei Huang (Graduate Student Member, IEEE) received the B.S. degree in communication engineering from Chongqing University, Chongqing, China, in 2019. He is currently pursuing the Ph.D. degree with the School of Electronics, Peking University, Beijing, China. His current research interests are high-mobility communication channel measurements and modeling. He was a co-recipient of IET Communications Best Paper Award: Premium Award.

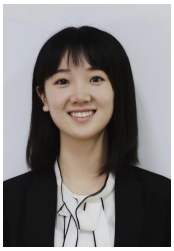

Lu Bai (Member, IEEE) (Member, IEEE) received the Ph.D. degree in Information and Communication Engineering from Shandong University, China, in 2019. From 2017 to 2019, she was also a visiting Ph.D. student at Heriot-Watt University, UK. From 2019 to 2022, she was a post-doc at Beihang University, China. She is currently a professor at Shandong University. Her general research interests are in areas of wireless communications and artificial intelligence, subject on which she has published more than 20 journal and conference papers, 2 books, holds 6 patents, and participated in 3 Chinese standards. Prof. Bai is a recipient of Qilu Young Scholar Award in 2022. She has served as the member of the Technical Program Committee and session chair for several international conferences. She is currently an Associate Editor of IET Communications.

Mingran Sun (Graduate Student Member, IEEE) received the B.S. degree in electronic and information engineering from Beihang University, Beijing, China, in 2023. He is currently pursuing the Ph.D. degree with the School of Electronics, Peking University, Beijing, China. His current research interest is Al-based channel modeling.

Xiang Cheng (Fellow, IEEE) received the Ph.D. degree jointly from Heriot-Watt University and the University of Edinburgh, Edinburgh, U.K., in 2009. He is currently a Boya Distinguished Professor of Peking University. His general research interests are in areas of channel modeling, wireless communications, and data analytics, subject on which he has published more than 280 journal and conference papers, 9 books, and holds 23 patents. Prof. Cheng is a recipient of the IEEE Asia Pacific Outstanding Young Researcher Award in 2015, a Distinguished Lecturer of IEEE Vehicular Technology Society, and a Highly Cited Chinese Researcher since 2020. He was a co-recipient of the 2016 IEEE JSAC Best Paper Award: Leonard G. Abraham Prize, and the 2021 IET Communications Best Paper Award: Premium Award. He has also received the Best Paper Awards at IEEE ITST'12, ICCC'13, ITSC'14, ICC'16, ICNC'17, GLOBECOM'18, ICCS'18, and ICC'19. He has served as the symposium lead chair, co-chair, and member of the Technical Program Committee for several international conferences. Prof. Cheng led the establishment of 3 Chinese standards (including 1 industry standard and 2 group standards) and participated in the formulation of 10 3GPP international standards and 2 Chinese industry standards. He is currently a Subject Editor of IET Communications and an Associate Editor of the IEEE Transactions on Wireless Communications, IEEE Transactions on Intelligent Transportation Systems, IEEE Wireless Communications Letters, and the Journal of Communications and Information Networks, and is an IEEE Distinguished Lecturer. In 2021 and 2023, he was selected into two world scientist lists, including World's Top 2% Scientists released by Stanford University and Top Computer Science Scientists released by Guide2Research.

Preben E. Mogensen (Member, IEEE) received the M.Sc. and Ph.D. degrees from Aalborg University, in 1988 and 1996, respectively. Since 1995, he has been a part-time Associate with Nokia. Since 2000, he has been a Full Professor with Aalborg University, where he is currently leading the Wireless Communication Networks section. He is also a Principal Scientist with Nokia Bell Labs and a Nokia Bell Labs Fellow. He has coauthored over 450 articles in various domains of wireless communication. His Google Scholar H-index is 68. His current research interests include the 5G industrial IoT and technology components towards 6G.

Xuesong Cai (Senior Member, IEEE) received the B.S. degree and the Ph.D. degree (with distinction) from Tongji University, Shanghai, China, in 2013 and 2018, respectively. In 2015, he conducted a three-month internship with Huawei Technologies, Shanghai, China. He was also a Visiting Scholar with Universidad Politécnica de Madrid, Madrid, Spain in 2016. From 2018-2022, he conducted several postdoctoral stays at Aalborg University and Nokia Bell Labs, Denmark, and Lund University, Sweden. He is currently an Assistant Professor in Communications Engineering and a Marie Skłodowska-Curie Fellow at Lund University, closely cooperating with Ericsson and Sony. His research interests include radio propagation, high-resolution parameter estimation, over-the-air testing, resource optimization, and radio-based localization for 5G/B5G wireless systems.

Dr. Cai was a recipient of the China National Scholarship (the highest honor for Ph.D. Candidates) in 2016, the Outstanding Doctorate Graduate awarded by the Shanghai Municipal Education Commission in 2018, the Marie Skłodowska-Curie Actions (MSCA) “Seal of Excellence” in 2019, the EU MSCA Fellowship (ranking top 1.2%, overall success rate 14%) and the Starting Grant (success rate 12%) funded by the Swedish Research Council in 2022. He was also selected by the “ZTE Blue Sword-Future Leaders Plan” in 2018 and the “Huawei Genius Youth Program” in 2021.